Rapid #: -8138834

CROSS REF ID: **1128573**

LENDER: **FUG :: Electronic Journals**

BORROWER: **COO :: Olin**

TYPE:	Article CC:CCG
JOURNAL TITLE:	International journal of modern physics A
USER JOURNAL TITLE:	International journal of modern physics. A, Particles and fields, gravitation, cosmology.
ARTICLE TITLE:	Electron cloud in accelerators
ARTICLE AUTHOR:	Roberto Cimino and Theo Demma
VOLUME:	29
ISSUE:	17
MONTH:	
YEAR:	2014
PAGES:	No pages in citation
ISSN:	0217-751X
OCLC #:	13191064

Processed by RapidX: 7/3/2014 8:54:41 AM

Review

International Journal of Modern Physics A
Vol. 29, No. 17 (2014) 1430023 (65 pages)

DOI: 10.1142/S0217751X14300233

Electron cloud in accelerators

Roberto Cimino

Laboratori Nazionali di Frascati, INFN,
via E. Fermi 40, Frascati, I-00044, Italy
roberto.cimino@lnf.infn.it

Theo Demma

Laboratoire de l'Accélérateur Linéaire,
CNRS-IN2P3, Université Paris-Sud 11, Orsay, F-91898, France
demma@lal.in2p3.fr

Received 18 March 2014
Accepted 2 April 2014
Published 13 June 2014

Low energy electrons in accelerators are known to interact with the circulating beam, giving rise to the formation of a so-called e^- cloud. Such e^- cloud may induce detrimental effects on the accelerated beam quality and stability. Those effects have been observed in most accelerators of positively charged particles. A longstanding effort has been so far devoted to understand in detail the physical origin of such e^- cloud, its build-up and its interaction with the circulating beam. We will first describe the origin and the basic features causing e^- cloud formation in accelerators, then we review some of the theoretical work produced to simulate and analyze such phenomenon. In selected cases, theoretical expectations and experimental observations will be compared, to address the importance of benchmarking codes versus observations to reach the required predictive capability. To this scope, codes need realistic input parameters which correctly describe material and surface properties at the basis of such e^- cloud formation and build-up. The experimental efforts, performed worldwide in many surface and material science laboratories, to measure such essential parameters will then be presented and critically reviewed. Finally, we will describe some of the e^- cloud mitigation strategies adopted so far and draw some conclusions.

Keywords: Accelerators; beam instabilities; e^- cloud formation; secondary electron yield.

PACS numbers: 29.20.−c, 79.20.Hx, 07.30.−t, 29.27.Bd

Contents

1. Introduction 2
2. Electron Cloud Build-Up 5
   2.1. Primary electrons 5
   2.2. Energy gain 7
   2.3. Electron multipacting 9

2.4. Cloud decay and electron survival . . . 12
2.5. Simulations . . . 13
2.6. The map approach . . . 16
3. Effects on the Beam . . . 18
3.1. Coherent tune shift . . . 19
3.2. Coupled bunch instability . . . 20
3.3. Single bunch instability . . . 22
4. Surface Parameters . . . 24
4.1. The secondary electron yield: Introduction . . . 25
4.2. Experimental for SEY studies . . . 28
4.3. Secondary electron yield of technical surfaces . . . 33
4.4. Low energy SEY . . . 35
4.5. Photoelectron yield . . . 38
4.6. Photon reflectivity (R) . . . 43
5. Countermeasures . . . 45
5.1. Coatings . . . 46
5.2. Solenoid field . . . 47
5.3. Electrodes . . . 49
5.4. Geometrical modification . . . 51
5.5. Electron and photon scrubbing . . . 52
6. Conclusions . . . 58
Acknowledgments . . . 58
References . . . 59

1. Introduction

The electron cloud phenomenon is a ubiquitous effect in accelerators of positive particles. First observations of related effects date back to nearly 50 years ago[1–4] and since then many different phenomena observed in many accelerators have been related to the formation of an electron cloud. The phenomenology of the e^- cloud formation together with the introduction of most relevant basic concepts, quantities and tools is analyzed in Fig. 1, in which we slightly modify the artistic view of the e^- cloud phenomenon for the case of a Large Hadron Collider (LHC) arc proposed by Francesco Ruggiero, head of the e^- cloud crash program launched at CERN in 1997.

The LHC arc dipoles have been described elsewhere[5–9] and are shown in Fig. 2. The interior of the dipole, see Fig. 2(b), is a complex and highly technological realization. Briefly, it consists of a cold bore held at 1.9 K hosting inside a so-called "beam screen," detailed in Fig. 2(c), held at temperature between 5 and 20 K, whose scope is essentially to protect the cold bore from unwanted heat deposition as caused by image currents, Synchrotron Radiation (SR), etc. The relevant LHC beam and chamber parameters are reported in Table 1. As soon as the first proton bunch appears in the dipole, see Fig. 1, being curved by the magnetic dipole field, it will emit SR. Those photons will travel tangentially to the beam orbit and hit the accelerator walls (around the orbital plane) with a very small grazing angle of incidence of about 1.5°. At this point they will be either reflected or absorbed by the wall. Some of the absorbed photons will produce photoelectrons, according to

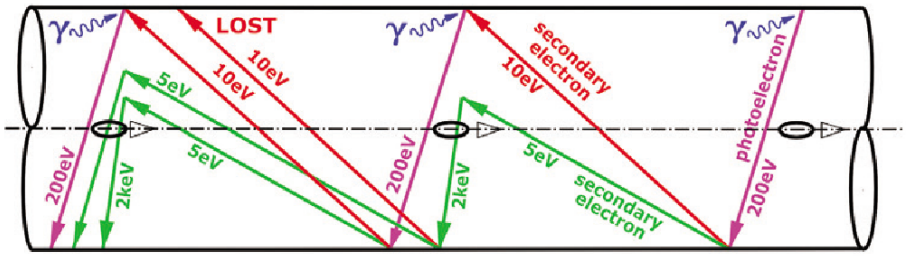

Fig. 1. Artistic view of the e^- cloud process at LHC (adapted from the original representation by F. Ruggero and in his memory).

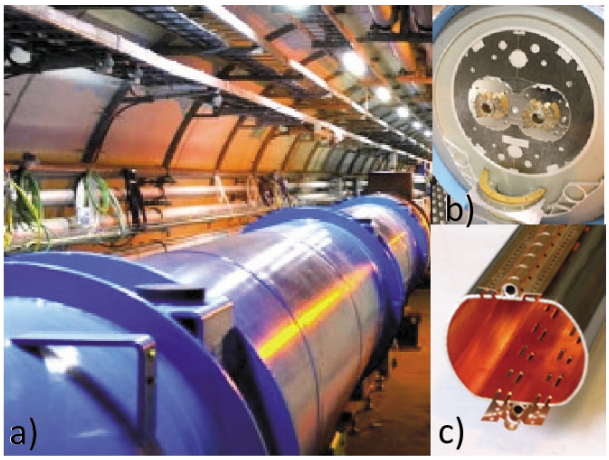

Fig. 2. (a) LHC tunnel; (b) inside of an LHC dipole; (c) Beam screen of an LHC dipole.[7]

the wall surface Photoelectron Yield (PY), i.e. the number of electrons produced per incident photon. The PY, of course, will depend on many parameters, like the actual photon energy, the angle of incidence, the surface roughness, etc. as discussed in Sec. 4. Here it is enough to just mention that the photoelectrons typically have very low energy, and once emitted travel very slowly in the accelerator beam pipe.

Such photoelectrons will then interact with the positive proton beam. It has to be noticed that photoelectrons are not the only possible seed to initiate the e^- cloud process. Electron cloud effects has been observed to occur also in CERN Proton Synchrotron (PS) and Super Proton Synchrotron (SPS),[11,12] where the SR produced by the protons accelerated at 450 GeV, has too low energy to generate photoelectrons. Any electron, coming from residual gas ionization is actually enough to initiate the process. Once electrons are emitted from the accelerator walls, they will see the beam and be, therefore, accelerated by Coulomb attraction. Some of them will be trapped by the beam but their limited velocity and their direction

Table 1. Typical LHC beam and chamber parameters for 50 and 25 ns bunch spacings.[10]

Parameter	Units	50 ns	25 ns
Beam particle energy	GeV	450–7000	
Bunch length	m	0.1124–0.075	
Transverse normalized emittances ($\epsilon_x = \epsilon_y$)	μm rad	3.5–3.75	
Number of bunches per train	—	36	72
Bunch gap at the end of each train	—	4	8
Number of trains in a batch	—	4	4
No. of particles per bunch N_b	10^{11}	1.15	
Bending field B	T	0.54–8.39	
Vacuum screen half height	mm	18	
Vacuum screen half width	mm	22	
Maximum SEY $\delta_{\max}$	—	2.2–1.1	
Energy for max. SEY $E_{\max}$	eV	230	

(being mainly normal to the beam and the walls) will then let them reach the accelerator wall again, once the beam is passed, as shown in Fig. 1. During such interaction with the beam, they do gain energy, once impinging against the opposite wall, they will generate a number of secondary electrons, whose intensity and energy distribution will depend on the beam pipe geometry, beam structure and on the Secondary Electron Yield (SEY) of the accelerator's material. SEY measures the number of electrons produced per incident electron at a given energy and, obviously, the higher it is the higher will be the number of electrons multiplied at each bunch passage. This is a resonant phenomenon, since the next bunches will not only create new photoelectrons but also accelerate towards the walls the electrons already present in the vacuum system. At some stage, then, the e^- cloud present will have such a high density to influence the actual beam quality at each passage, inducing detrimental effects, up to its complete degradation and loss. Other detrimental effects may also accompany the build-up of the e^- cloud, such as vacuum pressure rise, extra heat loads to the walls, etc. All those phenomena are known as e^- cloud effects, and are here called ECE. The electron multiplication, called multipactoring, can be carefully studied by simulations, which are an essential tool to address the e^- cloud problem. A number of sophisticated computer simulation codes have been developed to study ECE, and their predictions have been compared with experimental observations.

The basic concepts, quantities and tools related to the electron cloud formation introduced here will be discussed in more details, using the LHC dipole as an example, in Sec. 2. Then, in Sec. 3 some observed and/or simulated beam effects and instabilities related to e^- cloud, are discussed and emphasis is given to the effectiveness of the comparison between benchmarking simulations and observations to refine codes in order to obtain the required confidence in prediction capabilities. During the process towards the understanding of the e^- cloud phenomenon, it

has been more and more evident that an essential role is played by some relevant surface properties of the accelerator walls, calling for a huge experimental effort to study such essential issues in dedicated laboratory experiments. An attempt to summarize some of those results, will be given in Sec. 4. Finally, we will discuss, in Sec. 5, some active and proposed mitigation strategies. Open questions, further work and conclusions will be then presented in Sec. 6.

2. Electron Cloud Build-Up

The electron cloud phenomenology described in the introduction shows how this phenomenon is a consequence of a number of effects and is strongly dependent on the beam and on the actual accelerator material properties. In the following, we describe, in more details, each single step in the electron cloud build-up.

2.1. *Primary electrons*

Primary electrons are generated during a bunch passage, both on the wall, as photoelectrons from SR (mainly for positron or electron beams) and as secondary electrons generated by beam loss (especially for ion beams) and, inside the beam volume, by the ionization of the residual gas. The number of electrons created per unit length by SR or by beam loss during one bunch passage can become comparable to the average line density of beam particles, in which case these processes alone can give rise to appreciable ECE.

SR emission can be estimated starting from machine parameters (as described in many books[13,14]) and the energetics of such emitted spectrum is typically represented by the so-called "critical energy"[13,14] E_c which is the photon energy dividing the total emitted energy in two equal regions. The minimum photon energy needed to create a photoelectron from an irradiated surface strongly depends on the material work function (W), that is typically 3–5 eV. For electron (positron) machines such E_c can be as high as few KeV, showing how such accelerators produce a high number of photons that produce photoelectrons. Even in proton machines like LHC, it can be easily calculated that, at the nominal energy of 7 TeV, protons curved by a 8.4 Tesla dipole field, emit SR with a critical energy E_c of about 44 eV.[15,16] In Fig. 3, the photon flux produced in an LHC dipole is plotted for different energies of the beam and clearly shows that for energies above $\sim$2 TeV, the emitted photons are energetic enough to produce electrons. When such a white light (WL) distribution hits the wall of the beam chamber, it results in the production of photoelectrons at a rate that can be estimated as follows:

$$\frac{dN_{e\gamma}}{ds} \approx PY \frac{dN_\gamma}{ds} \approx PY \frac{5}{2\sqrt{3}} \frac{\alpha\gamma}{\rho}\,, \tag{1}$$

where the number of SR photons emitted in a dipole per unit length and per beam particle is $dN_\gamma/ds \approx 5\alpha\gamma/(2\sqrt{3}\rho)$, γ denotes the Lorentz factor, α the fine-structure constant and ρ the curvature radius of the particle trajectory. In general,

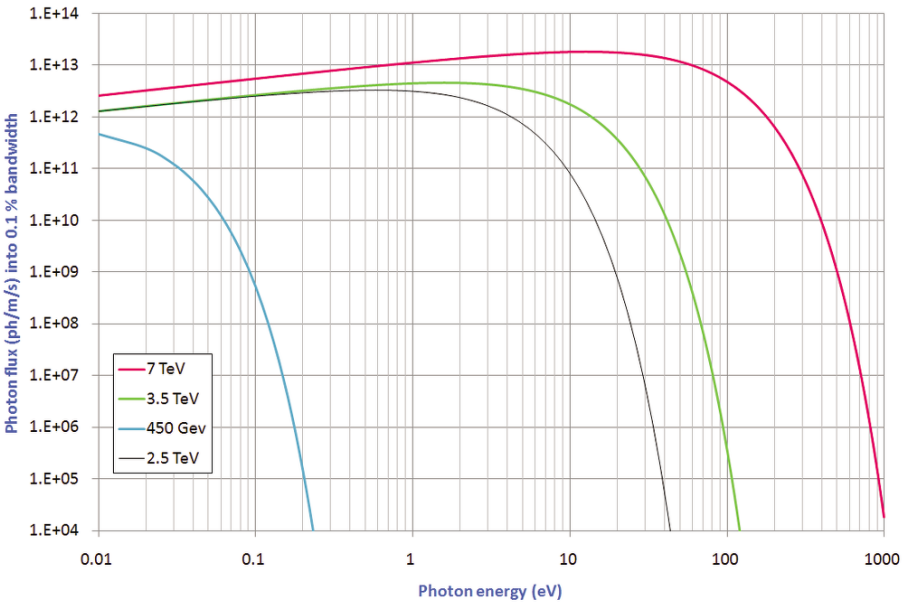

Fig. 3. (Color online) Synchrotron radiation spectra of an LHC dipole evaluated at different beam energies (green: 450 GeV; red: 3.5 TeV; blue: 7 TeV), using parameters in Table 1 and assuming a nominal beam current[25] $I = 584$ mA.

PY depends on the photon energy and angle of incidence and is a characteristic of the beam chamber material, as will be discussed in Sec. 4. Here, for simplicity, PY is a single parameter representing the total photon yield of the given SR spectrum. The azimuthal distribution of the photo-emitted electrons depends not only on the beam parameters but also on the shape and reflective properties of the chamber wall. The produced SR, with a given beam divergence, will illuminate the accelerator walls at a grazing incidence angle. Most of the photon beam will be scattered/reflected away, some will create photoelectrons, mostly in the presence of the dipole magnetic field perpendicular to the orbit plane but also outside the dipoles, in field-free regions. The electrons photo-emitted in the orbit plane, being affected by the magnetic field, are constrained to move along the field lines with very small cyclotron radius, thus they will not be able to cross the vacuum chamber and participate to the e^- cloud formation by gaining energy from the beam. On the other hand, the reflected photon beam will soon illuminate top and bottom walls, emitting photoelectrons perpendicular to the orbit plane (hence parallel to the magnetic field). Such photoelectrons will then spiral along the field lines, efficiently participating in secondary electron production and, eventually, in multipacting as all the photoelectrons created in field-free region. This simple reasoning shows how important it is to experimentally determine the photon reflectivity (R) of accelerator walls and its PY.[16–24]

If SR is not energetic enough to create photoelectrons, as in case of LHC at injection energy, residual gas ionization by beam particles becomes a possible source of primary electrons. The number of electrons produced per unit length by a bunch of N_b particles can be expressed as:

$$\frac{dN_{e,\,\mathrm{ion}}}{ds} = N_b \frac{P}{RT} \sigma_{\mathrm{ion}} \,, \tag{2}$$

where P is the pressure, T the temperature, R is the gas constant and σ_{ion} is the ionization cross-section. Typical values, valid for singly charged particles at ultra-relativistic energies, of the cross-section of for CO and N_2 gases are 1–2 Mbarn, and about 0.2 Mbarn for H_2 and other residual gases.[26] Considering LHC parameters one obtains from Eq. (2) that the production of primary electrons by ionization plays an essential role only at beam energies for which the photoelectron production is negligible (i.e. below $\sim$2 TeV).

Lost protons or ions impacting on the wall with a very grazing angle generate a large number of electrons. The SEY for ion impacting the surface with an angle of incidence θ with respect to the surface normal, is approximately given by[27]

$$Y_z \approx \Lambda \left(\frac{dE}{dx} \right)_e \cos^{-1}(\theta) \,, \tag{3}$$

where $(dE/dx)_e$ is the electronic stopping power of the material (expressed in MeV mg^{-1} cm^{-2}) and Λ is a phenomenological parameter, varying between 5 and 20 MeV mg^{-1} cm^2 assuming protons as projectiles. This mechanism is particularly important for heavy ions beam because of their high SEY[27] and in collimation regions in view of the high number of beam losses occurring there.

2.2. *Energy gain*

Electrons taking part in the e^- cloud build-up are nonrelativistic electrons ($v_e \ll c$) accelerated in the field of highly relativistic positive bunch ($\beta = v/c \approx 1$) moving in the longitudinal direction, z, of the beam pipe. The electric field of the relativistic bunch is Lorentz contracted to a cone with an angle of order $1/\gamma$ in the direction perpendicular to the beam's motion. Thus, as a first approximation, the influence of the longitudinal kick produced by the beam can be neglected because its effect is small together with all the bunch related magnetic effects. First, consider the case in which a Gaussian bunch is approximated by a uniformly charged cylinder of radius σ_r and constant linear density

$$\lambda_b = \frac{N_b}{\sqrt{2\pi}\sigma_z} \,, \tag{4}$$

where N_b is the number of charged particles in the bunch and σ_z the bunch length. Assuming a perfectly conducting cylindrical beam pipe, the electric field generated

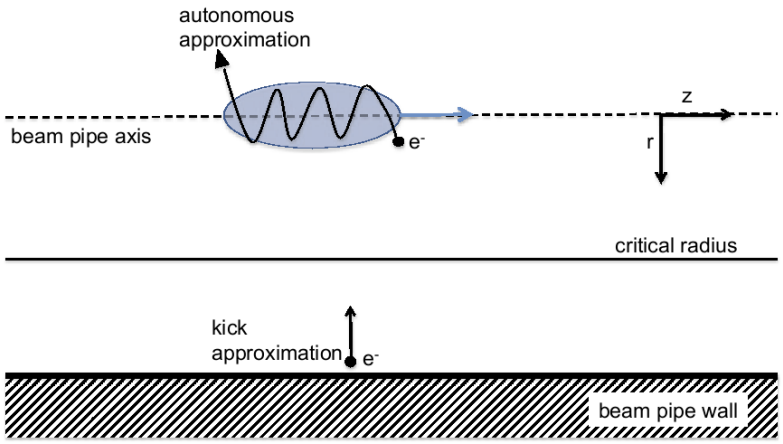

Fig. 4. Electron-bunch interaction regimes in a cylindrical beam pipe.[28]

by the bunch is purely radial and assume the form:

$$\vec{E}(r, z-\beta ct) = \begin{cases} \dfrac{\lambda_b}{4\pi\epsilon_0\sigma_r^2}\vec{r}\,\Pi\left(\dfrac{z-\beta ct}{\sqrt{2\pi}\sigma_z}\right) & \text{for } r \le \sigma_r\,, \\ \dfrac{\lambda_b}{2\pi\epsilon_0}\dfrac{\vec{r}}{r^2}\,\Pi\left(\dfrac{z-\beta ct}{\sqrt{2\pi}\sigma_z}\right) & \text{for } r \ge \sigma_r\,, \end{cases} \tag{5}$$

where $\Pi(x)$ is the rectangular window function. It is possible to distinguish two regimes as a function of the initial electron position.[28] The "kick" regime corresponds to the electrons outside the beam core that are nearly stationary during a bunch passage. The "autonomous" regime corresponds to electrons that get trapped within the beam core. The critical radius r_C separating these two regimes is defined as the radial distance for which the time for the bunch to pass is equal to a quarter of the oscillation period. It can be calculated as

$$r_C \approx 2\sqrt{N_b r_e \sigma_z \sqrt{\frac{2}{\pi}}}\,, \tag{6}$$

where r_e is the classical radius of the electron. A schematic view of the electron-bunch interaction is presented in Fig. 4. The energy gained by the electrons in the kick regime is readily obtained from Eq. (5) as:

$$\Delta E_{\text{kick}} = 2m_e c^2\left(\frac{N_b r_e}{r}\right)^2. \tag{7}$$

For an electron created at time t_0 after the head of the bunch passed by, the momentum gain has to be scaled by a factor $(\Delta t_b - t_0)/\Delta t_b$, where Δt_b is the time it takes for the bunch to pass. Electrons trapped inside the beam core performs

harmonic oscillations of frequency:

$$\omega_e = c\sqrt{\frac{2\pi r_e N_b}{\sigma_r^2 \sigma_z}}\,. \tag{8}$$

The energy gained by such electrons depends on the exact period of the oscillation, the time that the particle is subjected to the force, and its energy at the start of the oscillation. For an electron initially at rest at a distance equal to the transverse size of the bunch, the energy gain is:

$$\Delta E_{\text{bunch}} = \frac{1}{2} m_e \omega_e^2 \sigma_r^2 = \frac{1}{2} m_e c^2 \frac{r_e N_b}{\sigma_z}\,. \tag{9}$$

More realistic scenarios have been considered in Ref. 28 and take into account that:

- the electrons are not stationary, but move during the bunch passage.
- the bunch charge spatial distribution is longitudinally and transversely non-uniform.

The obtained estimations of the energy gain as a function of the initial radial position of the particle for nominal LHC parameters and various bunch shapes are shown in Fig. 5. As a final example, we show in Fig. 6, the electron energy distribution (red curve) gained after a single bunch passage, for an LHC dipole, as obtained with the code ECLOUD.[29] Calculations assume an initial photoelectrons energy distribution (blue curve in Fig. 6) modeled as a truncated Gaussian centered at 7 eV, with a standard deviation of 5 eV, based on experimental findings[16] discussed in Sec. 4. The electrons in the chamber gain energy but maintain a significant density at very low energies.

2.3. *Electron multipacting*

The primary mechanism causing a build-up of electrons is beam induced multipacting. Here electrons accelerated by the electric field of the passing bunches hit the vacuum chamber wall with such an energy to produce, on average, more than one secondary electron per incident one. The number of secondary electrons depends on the SEY of the chamber material, which is a function of the primary electron energy, its angle of incidence, and the chamber surface composition and history. SEY measures the capability of a solid surface to produce secondary electrons, once it is irradiated by electrons of different primary energy, and is commonly denoted by $\delta(E)$.[30] $\delta(E)$ can be actually measured in laboratory experiments and some of such results will be discussed in Sec. 4. The typical behavior of the SEY as a function of the energy of the impinging electron is reported in Fig. 7, where $E_{\max}$ is the value of the energy at which the SEY assumes its maximum values $\delta_{\max}$, and E_1 and E_2 are the extrema of the energy interval in which $\delta(E) > 1$. In simulation codes, the SEY curve is simplified to a curve depending on few input parameters like $\delta_{\max}$, $E_{\max}$ and δ_0. Such parametrization may mask some of the effects that could be

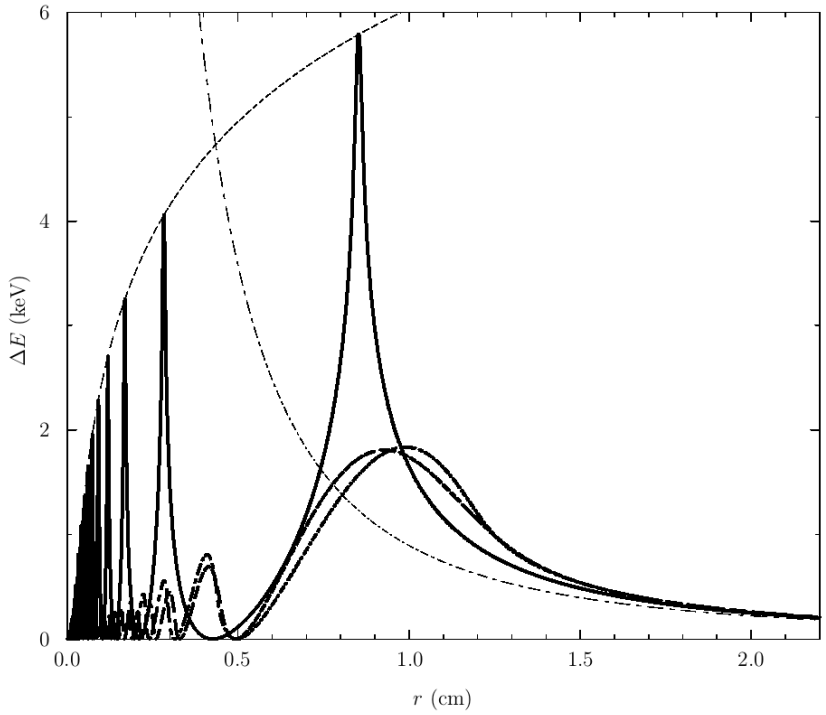

Fig. 5. Energy gain as a function of initial particle radius for the nominal LHC parameters. The solid line is for a rectangular bunch, the dashed line is for a Gaussian bunch, and the dot–dashed line is for a parabolic-like bunch. The thin dashed line shows what the maximum energy gain is expected to be in the autonomous approximation, whereas the thin dot–dashed line is the energy gain expected in the kick approximation (from Ref. 28).

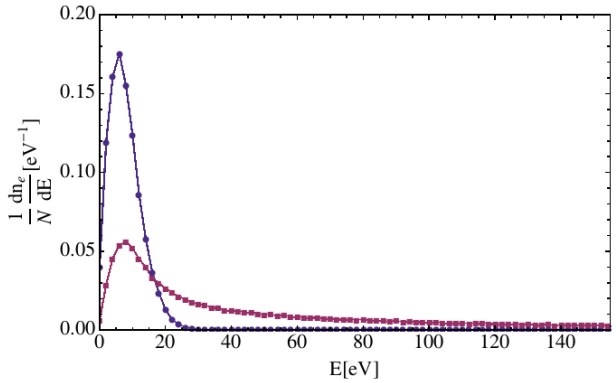

Fig. 6. (Color online) Photoelectron energy distribution at the moment of emission (blue) and after the first bunch passage (red) as computed by the code ECLOUD for an LHC dipole using parameters collected in Table 1.

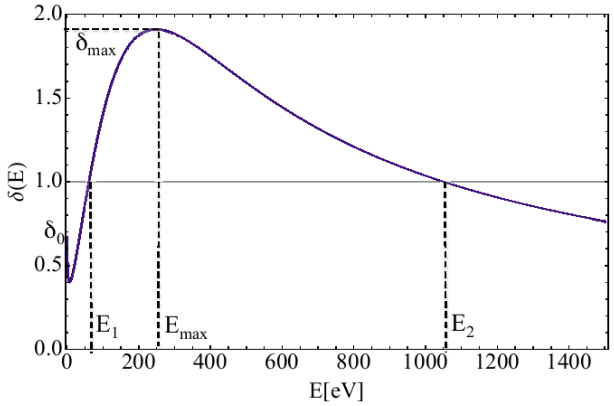

Fig. 7. Typical behavior of the secondary electron yield as a function of the impinging electron energy. The behavior changes for different materials, with different $\delta_{\max}$, $E_{\max}$, E_1, E_2, δ_0, etc.

predicted in simulations due to subtle variation of the actual SEY shape, as seen to occur in experimental runs (see Sec. 4).

For bunched beam, induced multipacting could be interpreted as a resonance phenomenon. In particular, a multiplication of the secondary electrons takes place if the electrons produced and accelerated during the passage of a bunch cross the beam chamber and hit its walls with impact energy between E_1 and E_2, producing secondaries in coincidence of the passage of the following bunch. In absence of an external magnetic field, for a round chamber of radius b and short bunches of N_b particles, spaced by s_b, and assuming that the primary electrons are produced on the wall (e.g. through photoemission) with low energy $E \ll \Delta E_{\text{wall}}$, this resonance condition takes the simple form:[31]

$$N_b r_e s_b = b^2 \,. \tag{10}$$

If this condition is fulfilled, at every bunch passage not only new primary electrons will be created and accelerated in order to produce secondaries but also all the secondaries produced by previous bunches will be accelerated by the beam leading to an exponential growth of the electron density. However both simulation and experimental observation show that condition (10) is too stringent. In reality, the secondary electrons are produced with an energy distribution that is peaked at very low energy (see Sec. 4.3) and they could travel in the vacuum chamber for a long time after a bunch passage. Therefore, most of the secondary electrons may not yet be lost when the next bunch arrives and these electrons will be accelerated during its passage, producing a new generation of secondaries. On the other hand, for bunch spacing shorter than that suggested in (10), electrons can interact with several passing bunches, and, also in this case hit the wall with an energy between E_1 and E_2 inducing the multipacting process. However, the electron multiplication is not unlimited. At a certain level of the cloud density, the number of new

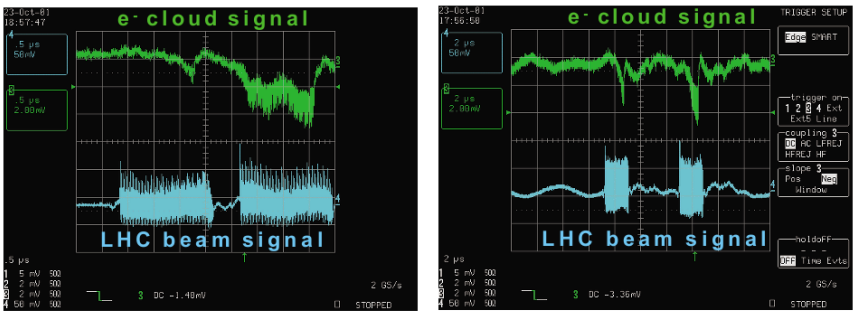

Fig. 8. Pickup signal of the cloud build-up of two SPS batches composed of 72 bunches, spaced by 550 ns (left panel) and by 5.25 μs (right panel). From Ref. 35, thanks to M. Jimenez.

electrons produced through the primary or secondary emission process will be equal to the number of electrons that are absorbed by the beam chamber leading to a quasi-stationary equilibrium. The level of density at which this quasi-stationary equilibrium is reached strongly depends on the beam and chamber parameters and if the multipacting process occurs. In general, if multipacting occurs the e^- cloud density grows exponentially until the equilibrium is reached under the influence of the space charge field of the cloud itself. Several models[32–34] have been developed in order to find simple analytical expressions for the multipacting threshold and the equilibrium density. These models, invoking several approximations and *ad hoc* assumptions, are very useful to have a deeper comprehension of the dependence of the e^- cloud dynamics on the relevant parameters in some particular cases but they are not (still) capable to give general and reliable predictions such as numerical simulations can do.

2.4. *Cloud decay and electron survival*

The electron density decays in the gap between bunch trains. Experimental observations shows that such decay is much slower then expected[35,36] and a sort of memory effect seems to occur. This behavior is shown in Fig. 8 where the pickup signal of the cloud build-up of two SPS batches, composed of 72 bunches, spaced by 550 ns shows that the cloud signal is much more ready to start during the passage of the second batch. Several effects are suspected to contribute to the long memory and lifetime of the electron cloud: nonuniform fields, such as quadrupoles or sextupoles, may act as magnetic bottles and trap electrons for an indefinite time period;[37,38] if the SEY in the limit of zero electron energy δ_0 approaches 1, as is suggested by some measurements,[39] low energetic electrons could survive nearly forever, bouncing back and forth between the chamber walls; ions due to ionization of the residual gas or debunched (coasting) beam may focus the e^- cloud even in the absence of the beam.[62]

2.5. *Simulations*

The simulation or the e^- cloud build-up is performed following the steps described in the previous sections. Typically build-up codes make the approximation that the beam is a prescribed function of space and time while the electrons of the cloud are grouped in Macro Particles (MP). With this assumption, it is possible to study the evolution of the e^- cloud but not its effect on the beam. The steps performed in a build-up simulation can be summarized as follows:

- At each time step, a certain number of primary MP's are generated accordingly to the mechanism of primary production (e.g. ionization of residual gases and/or photoemission).
- The total electric field acting on each MP is computed as the sum of the field generated by the beam and the space charge field of the e^- cloud itself. Typically these fields are computed by the Particle In Cell (PIC) algorithm.[40] When possible, in particular for the beam contribution to the total field, analytical expressions are used to speed up the computations.
- The equations of motion taking into account the computed electric field and the external magnetic fields (if present) are integrated and the positions and momenta of the MP's are updated accordingly.
- At each time step, the MP's hitting the wall are identified and a secondary emission process is applied in order to generate the emitted electrons.

Based on these steps several build-up codes have been developed.[29,37,41–47] Historically, the first modern electron cloud simulation code was developed in 1995 by Ohmi,[48] first e^- cloud simulations for PEP-II were presented by Furman and Lambertson in 1996,[41] and the first electron cloud simulation for the LHC by Zimmermann in 1997.[43] Today the most used electron cloud build-up codes are POSINST,[41,42] ECLOUD,[29,43] CLOUDLAND[37,45] and PyECLOUD.[46] Each one of this codes implements different algorithms, based on theoretical or empirical models, for the production of primary and secondary electrons, different routines for tracking MP's and compute the space charge field. A comprehensive online repository containing code descriptions and contact persons has been developed by the CARE program.[49] As an example of application of these codes, we used the code ECLOUD to simulate the electron cloud formation in an LHC dipole, using the parameters listed in Table 1 assuming an energy of 7 TeV, a bunch spacing of 25 ns and uniform distribution of the photons reflected in the beam chamber. The typical time evolution of the electron cloud line density is shown in Fig. 9, for a filling pattern consisting of a train of 72 bunches followed by gaps of 28 empty (zero-charge) bunches. The two plots corresponds to $\delta_{\max} = 2$ (left panel) and $\delta_{\max} = 1$ (right panel). In the case of $\delta_{\max} = 2$, multipacting takes place and, except for superimposed oscillations, the density grows exponentially in time as more and more bunches pass by, until an equilibrium is reached. The subsequent decay corresponds to the successive passage of the empty bunch train.

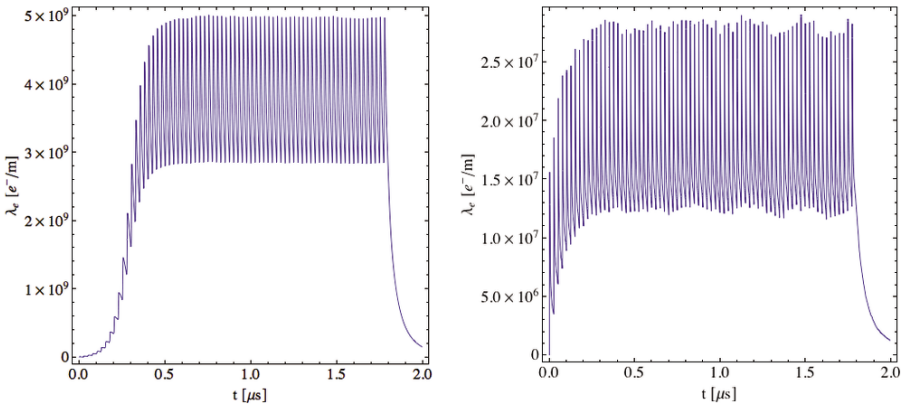

Fig. 9. Evolution of the electron density computed with ECLOUD. The case shown corresponds to a filling pattern featuring 72 charged bunches, with bunch charge of $N = 1.0 \times 10^{11}$ protons, followed by 28 empty (zero-charge) bunches. The assumed bunch spacing is 7.48 m, and the maximum value of the SEY is $\delta_{\max} = 2.0$ (left) and $\delta_{\max} = 1.0$ (right).

In the case $\delta_{\max} = 1$, mulitpacting is not observed, the photoelectrons emitted by the wall surface are quickly reabsorbed by the beam chamber leading to a much lower saturation level. In bending magnets, the EC distribution develops characteristic geometrical patterns. For a magnetic field $B = 8$ T and typical EC energies < 100 eV, the electrons move in spiral trajectories about the field lines with radius < 5 μm. Thus, in practice, the electrons are free to move only in the vertical direction and the vertical kick imparted by the beam on a given electron depends on the horizontal coordinate. Hence it can happen that at a particular horizontal location inside the beam chamber, the electrons hit the wall with energy close to $E_{\max}$, leading to characteristic high density vertical stripes symmetrically located around the center of the chamber.[50] A snapshot of the spatial distribution of the electron cloud computed "just before" the passage of bunch 72 is shown in Fig. 10 where the stripes structure of the electron cloud is evident. Similar calculations can generate the spatial distribution in different magnetic field configuration. Figure 11 shows an example of such distributions in the case of a field free region, a solenoidal field and a quadrupole field using the SuperB machine parameters.[51] In free field regions, the electron are attracted towards the bunch and the cloud distribution is pinched. In a longitudinal solenoidal field, electrons are forced onto circular orbit remaining confined near the wall. In a quadrupole, the electron distribution exhibits a characteristic fourfold stripes pattern. Similarly, build-up codes can simulate the energy distribution of the cloud electrons hitting the wall. As an example, we show in Fig. 12, the accumulated normalized energy distribution curve (EDC) of electrons hitting the LHC dipole inner chamber is shown for the nominal 25 ns bunch filling pattern using parameters listed in Table 1. The black curve is obtained for $\delta_{\max} = 2$, while the red one for $\delta_{\max} = 1$. In both cases, the number of electrons with

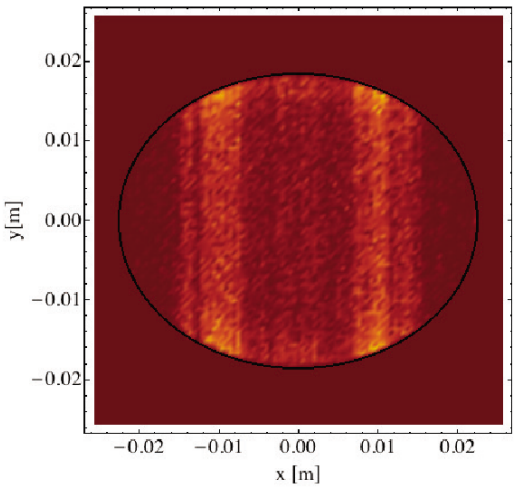

Fig. 10. Snapshot of the normalized electron cloud density at saturation for an LHC dipole.

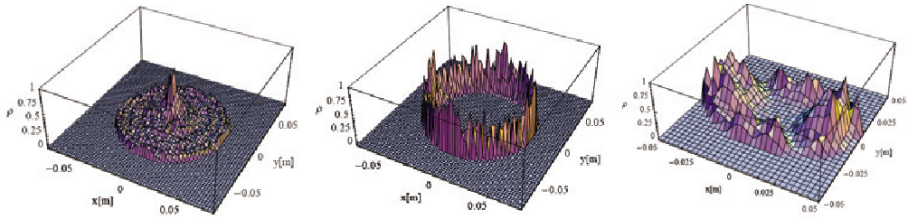

Fig. 11. Snapshots of the normalized electron cloud density at saturation for a drift, solenoid, and quadrupole using the SuperB machine parameters.[51]

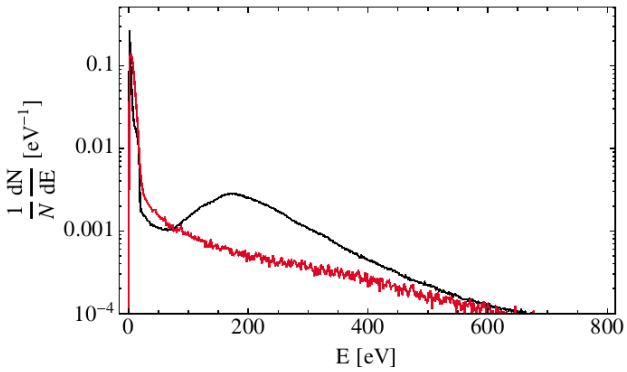

Fig. 12. (Color online) Accumulated energy distribution of the electrons hitting the wall after the passage of a nominal 25 ns bunch filling pattern as computed with the code ECLOUD for an LHC dipole using parameters listed in Table 1. The two curves correspond to $\delta_{\max} = 2$ (black) and $\delta_{\max} = 1$ (red).

low energy (in Fig. 12 $E < 20$ eV) is an order of magnitude higher than the high energy ones. In the case of $\delta_{\max} = 2$ for which multipacting occurs, a peak of the energy distribution around $E_{\max} = 230$ eV is observed while in the $\delta_{\max} = 1$ case, the 20 eV separation line divides the plot into two nearly equally populated regions.

As we have seen, the electron cloud evolution strongly depends on a wide range of parameters that are not all well-known *a priori*. The main parameters that are not well known are those related to various surface properties like photon reflectivity; photoemission yield or quantum efficiency (PY), photoemission spectrum, and SEY and spectrum. Hence comparing and benchmarking electron cloud build-up simulation codes is a key ingredient to better understand the phenomena. Typically results of simulations performed over a range of one or more input parameters are compared with measurements. By iterating this process, e^- cloud related parameters that are not well known can be extrapolated. One of the first examples of the application of this procedure was used in Ref. 52 to extract $\delta_{\max}$ and δ_0 comparing the ECLOUD simulation results obtained for a set of such parameters with measurements of electron flux at the wall with a strip detector in the SPS. In this way, the parameters giving the best fit to the observation were assumed to be the best estimate of the otherwise unknown parameters. Since then, similar procedures have been used to compare simulation predictions with a variety of observables including: signals from Retarding Field Analyzers,[53] Beam Position Monitors,[54] pressure,[55] heat load,[56] microwave dispersion measurements,[57] etc. As an example, Fig. 13 shows measured and simulated signals, where the simulated signal, obtained with $\delta_{\max} = 1.6$ and $\delta(0) = 0.5$, was low pass filtered with a corner frequency of 200 MHz. The impressive resemblance between the two curves suggests that the assumed electron cloud model correctly describes the phenomenon.

2.6. *The map approach*

The analysis performed so far was based on very heavy computer simulations taking into account photoelectron production, secondary electron emission, electron dynamics, and space charge effects providing a very detailed description of the electron cloud evolution. In Ref. 58, it has been shown that, for the typical parameters of the Relativistic Heavy Ion Collider (RHIC), the evolution of the linear electron cloud density can be followed from bunch-to-bunch introducing a "cubic map" of the form:

$$\rho_{m+1} = \alpha\rho_m + \beta\rho_m^2 + \gamma\rho_m^3\,, \tag{11}$$

where ρ_m is the average electron cloud density after mth passage of bunch. The coefficients α, β, γ are parameters extrapolated from simulations, and depends on beam and beam pipe parameters. The linear term describes the growth and its coefficient α has to be larger than unity in case of electron multipacting; the quadratic term describes the parabolic decay due to saturation effects, therefore β has to be negative to give concavity to the curve ρ_{m+1} versus ρ_m; the cubic term

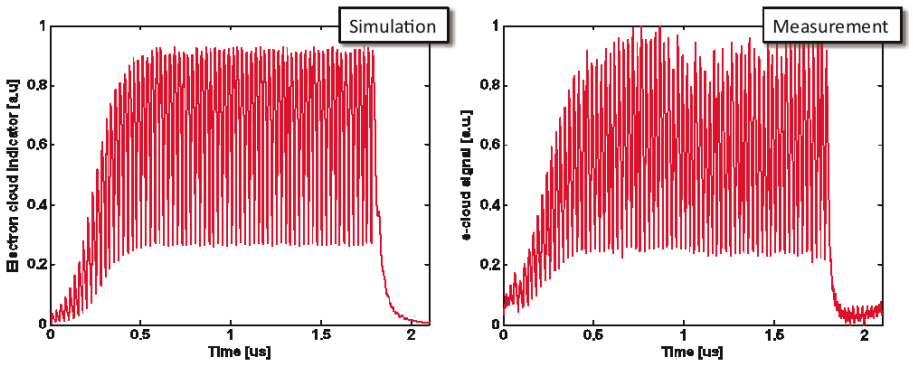

Fig. 13. e^- cloud build-up simulation (left) and measurement (right) for a 25 ns beam with 1.33×10^{11} ppb and 4 ns long. From Ref. 12, thanks to G. Iadarola and G. Rumolo.

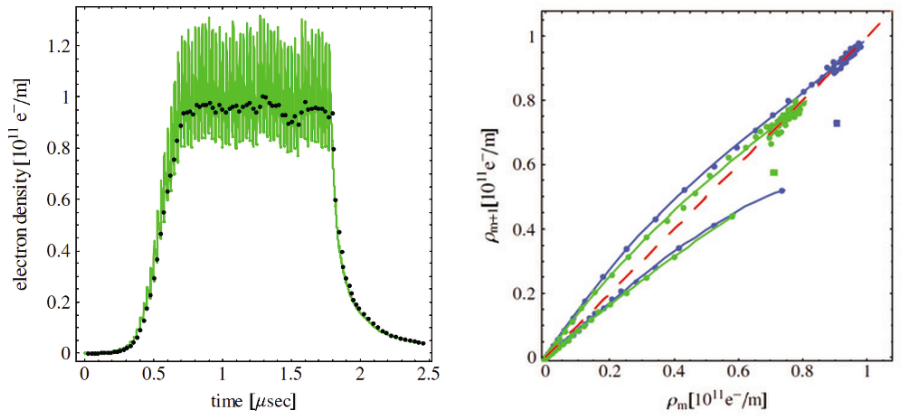

Fig. 14. (Color online) Left: evolution of the electron density (green line) computed with ECLOUD. The case shown corresponds to a filling pattern of 72 charged bunches, with bunch charge $N = 1.0 \times 10^{11}$ protons, followed by 28 empty (zero-charge) bunches. The assumed bunch spacing is 7.48 m, and $\delta_{\max} = 1.5$. The black markers identify the average electron density between two consecutive bunches. Right: Average e^- cloud density map ρ_{m+1} versus ρ_m. Circle markers: ECLOUD simulations ($\delta_{\max} = 1.5$). The dashed red line represents saturation ($\rho_{m+1} = \rho_m$). Markers above the saturation line describe the e^- cloud build-up (cyan: $N = 1.6 \times 10^{11}$; green: $N = 0.8 \times 10^{11}$). Markers below the saturation line describe the e^- cloud decay. The cyan and green lines are the corresponding cubic fits. Transitions between filled and empty bunch trains are shown as square markers. From Ref. 59.

corresponds to perturbations. Such a map approach has been proved, by numerical simulations, reliable also for LHC dipoles.[59] The working principle of the map approach is shown in Fig. 14. In the left panel, one can see that the bunch-to-bunch evolution contains enough information about the build-up and the decay time, although the details of the electron density oscillation between two bunches are lost. The right panel of Fig. 14 shows the average e^- cloud density between two

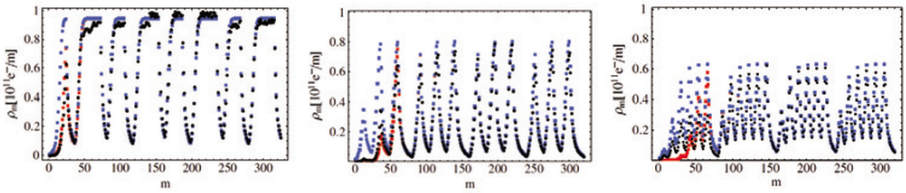

Fig. 15. (Color online) Average e^- cloud density evolution for three different bunch-train filling patterns, for $N = 1.2 \times 10^{11}$ and $\delta_{\max} = 1.7$. Left: $24f - 12e - 36f$; mid: $3 \times (12f - 12e)$; right: $6 \times (6f - 6e)$. In both cases, successive bunch trains are separated by gaps whose length corresponds to 28 (empty) bunches. Black markers: ECLOUD results. Blue and red markers: map results corresponding to initial electron densities $\rho_0 = 10^9[e^-/m]$ and $\rho_0 = 10^7[e^-/m]$, respectively (adapted from Ref. 59).

bunches using results from ECLOUD, the lines are cubic fits of these points. The dynamics of electron cloud is explained as follows. Starting with a small initial linear electron density, after some bunch passages, the density takes off and reaches the corresponding saturation line ($\rho_{m+1} = \rho_m$, red line). In this situation, all the points are in the same spot. Neglecting the point corresponding to the e^- cloud density after the first empty bunch, the longitudinal electron density follows a similar decay independently of the initial value of the saturated line electron density. Thus the electron density for a given set of parameters is described by two cubic maps, one for the build-up and one for the decay. Cubic fits can be used also for the description of the transition points.[58] The key property of the map is that, for all practical purposes, its coefficients do not depend on the bunch filling pattern, and thus they can be deduced from only one time-consuming simulation. As an illustration of this important property, the agreement between ECLOUD and map predictions is clearly shown in Fig. 15 (displaying the time evolution, ρ_m versus m). The reduction in the computing time is several orders of magnitude. Furthermore, in Ref. 60, it has been proved that the map formalism can be applied to the bunch-by-bunch electron flux at the wall and in Ref. 61, this method has been applied to the optimization of the LHC bunch filling pattern to maximize the electron flux while taking the e^- cloud electron density below a prescribed value.

Even though the behavior of the map coefficients, once extrapolated from simulations, gives an accurate description of the bunch-by-bunch e^- cloud evolution, their dependence on beam and beam pipe parameters is not completely understood. An analytical expression of the linear coefficient α has been given in Ref. 63 for a field free region and in Ref. 64, for a dipole. Work is in progress to find an analytical expression also for the higher order terms in the maps.[65]

3. Effects on the Beam

Once an electron cloud is formed, it interacts with the beam. Depending on the e^- cloud density, the interaction could result in many detrimental effects on the beam such as: coherent tune shift, coupled bunch instability and single bunch instability.

Those effects will then induce emittance growth, decrease of ben lifetime, and will ultimately lead to beam loss. In this section, we briefly review both the analytical and numerical model for the description of the beam-cloud interaction.

3.1. *Coherent tune shift*

Let us assume an initial electron density, prior to the bunch passage, ρ_e constant along the ring. Such electron distribution generates an electric field acting on the positive charged beam as a supplemental focusing force. Therefore the betatron tune of the beam is shifted by:[66]

$$\Delta Q \approx \frac{r_{\rm cl}}{2\gamma}\bar{\beta}\rho_e C\,, \tag{12}$$

where $\bar{\beta}$ is the average beta function, C is the ring circumference, γ is the beam Lorentz factor, and $r_{\rm cl}$ is the classical beam particle radius. As seen in the previous section, the density ρ_e varies in time together with the induced tune shift. Bunch-by-bunch tune shift increasing along the bunch trains is characteristic of the presence of an e^- cloud and has been measured in all the machines affected by ECE. This measurement can be used as a benchmark for simulation codes. In particular, in Cesr-TA a large variety of coherent tune shift data have been taken, covering a wide range of beam and machine conditions. We present in Fig. 16, a comparison between measured and simulated tune shifts. The contribution to the bunch-by-bunch tune shifts from drift and dipole beamline elements have been

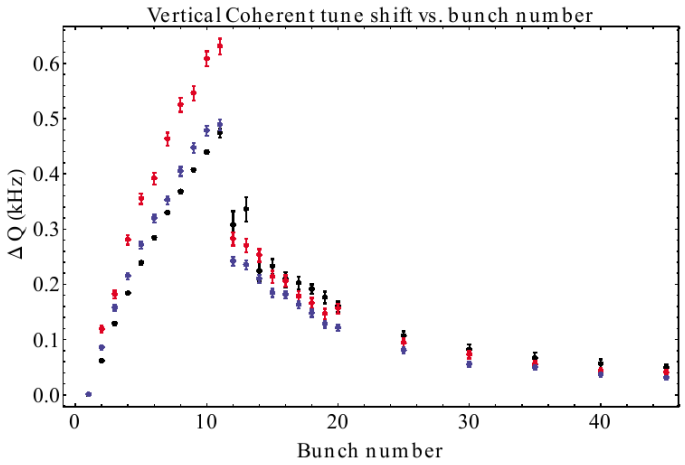

Fig. 16. (Color online) Measured vertical tune shift (black points) versus bunch number, for a train of 10 positron bunches, with 0.75 mA/bunch at 5.3 GeV spaced by 14 ns, followed by witness bunches at various spacings. Red points are computed (using POSINST) based on direct radiation and an *ad hoc* assumption about the scattered photons. Blue points, which are in better agreement with the data, are computed using results from Synrad3D as input to POSINST. From Ref. 68, thanks to G. Dugan.

computed from the electric field gradients of the charge distributions predicted by the electron cloud simulation codes. The ring-wide average tune shifts were then calculated by taking a β-weighted average of the field gradients per beamline element, and compared with measurements. Quite a good agreement[67] has been found between the measurements and the computed tune shifts, using both the build-up codes POSINST and ECLOUD. This agreement, which is found for the same set of simulation parameters applied across a wide variety of machine conditions, both constrains many of the model parameters and gives confidence that the models do in fact predict accurately the correct build-up of the electron cloud measured in Cesr-TA.

3.2. *Coupled bunch instability*

In multibunch operation, the presence of the Electron Cloud can correlate the motion of the bunches with each other. When the beam passes through the cloud, bunches interact with it. If one bunch is displaced with respect to the center of symmetry of the cloud then an asymmetry is induced on the electron distribution. This asymmetry could last long enough to kick the following bunches. Hence even small betatron oscillations of one bunch couple to the motion of other bunches via the electron cloud, resulting in a coupled bunch instability. Multibunch instabilities driven by an electron cloud were observed with positron beams at the KEK Photon Factory,[69] at BEPC,[70] at KEKB,[71] at PEPII[41] and at DAΦNE[72] as well as with proton beams at the CERN SPS.[73] A simplified analytical model of the multibunch instability was developed in Ref. 48.

Ignoring the internal structure of the bunches and assuming N_p equi-spaced Gaussian bunches, the beam-electron cloud system is described by the following equations:[71]

$$\frac{d^2\mathbf{x}_p}{ds^2} + K(s)\mathbf{x}_p = \frac{2N_e r_e}{\gamma}\sum_{e=1}^{n_e}\mathbf{F}(\mathbf{x}_p - \mathbf{x}_e)\delta_P(s - s_e)\,, \tag{13}$$

$$\frac{d^2\mathbf{x}_e}{dt^2} = \frac{e}{m_e}\frac{d\mathbf{x}_e}{dt}\times\mathbf{B} - 2N_p r_e c\sum_{p=1}^{N_p}\mathbf{F} \times (\mathbf{x}_e - \mathbf{x}_p)\delta_P(t - t_p(s_e)) - r_e c^2\frac{\partial\phi(\mathbf{x}_e)}{\partial\mathbf{x}_e}\,, \tag{14}$$

where $\mathbf{x}$ and s denote the transverse and longitudinal positions, subscripts p and e denote positron and electron, respectively, r_e is the classical electron radius, m_e is the electron mass, c is the speed of light, e is the electron charge, δ_P is the Dirac delta function, $\mathbf{F}$ is the Coulomb force in two-dimensional space given by the Bassetti–Erskine formula,[74] and ϕ is the electric potential due to electrons satisfying the Poisson equation. Ordinary instability theory is based on the wake formalism.[75] If linearity and superposition are satisfied, the vertical force experienced by a bunch at z can be expressed by the convolution of the wake field $W(z)$ and the dipole

moments of the preceding bunches in the train ($z_i < z_j$):

$$F_y = \frac{N_p r_e}{\gamma} \sum_{j>i}^{\infty} W(z_i - z_j) y_j(z_j)\,, \tag{15}$$

the same relation with y substituted by x holds for the horizontal direction. The coherent multibunch oscillation frequency can be computed from the wake function $W(z)$ using standard first-order formulas:[71,75]

$$(\Omega_m - \omega_\beta)L/c = \frac{N_p r_e \beta}{2\gamma} \sum_{l=1}^{N_w} W(-l s_b) \exp\left(2\pi l i \frac{m + \nu_\beta}{H}\right), \tag{16}$$

where N_w represents the range of the wake function. The imaginary part of $\Omega_m L/c$ gives the growth rate of the mth mode for H equi-spaced bunches characterized by bunch oscillations:

$$y_m(z_j) = a \exp(-i\Omega_m t + 2\pi i m j/H)\,. \tag{17}$$

At a position s along the ring the variation of the momentum $y' = dy/ds$ of the ith bunch due to the interaction with the perturbed cloud is:[71]

$$\Delta y'_{p,i} = \frac{N_p r_e}{\gamma} \sum_{j>i}^{i+N_w} W(z_i - z_j) y_{p,j}\,. \tag{18}$$

This last relation can be used to extrapolate the wake $W(z)$ from simulation codes:[41,41,71] the evolution of the cloud is followed as long as a saturation level is reached, then a bunch is displaced by a certain amount in the transverse plane and the momentum kicks received by the following bunches are registered. Finally the system of equations (18) is solved to obtain $W(z)$. Simulations of the multibunch wakefields based on Eq. (18) were reported first by Ohmi in Ref. 48 and further refined in Ref. 41. Direct simulations of the instability, based on a self-consistent numerical integration of the two coupled equations (22) and (23), were presented in Ref. 71. Figure 17 shows the measured (top-left) and simulated (top-right) horizontal mode spectrum for KEKB together with two snapshot of the beam electron motion. The good agreement between simulation and measurements is quite clear and it was possible to conclude that the instability is due to the coherent mutual oscillation of the beam and the cloud itself. For this reason, the coupled bunch instability strongly depends on the spatial distribution of the electron cloud. As an example in DAΦNE, a strong horizontal instability has been observed.[72] The most unstable mode observed is always the slowest one, characterized by an oscillation frequency $f = (1 - \nu_x) f_0$, where ν_x is the fractional part of the horizontal tune and f_0 is the revolution frequency. This mode also corresponds to the most unstable mode induced by a resistive wall wake field and is often referred as the $m = -1$ mode. DAΦNE is a very compact ring where magnets occupy almost all its circumference. Simulations[72] suggest that the electrons in bending magnets and damping wiggler are dominant in the instability mechanism, also in view of the very high

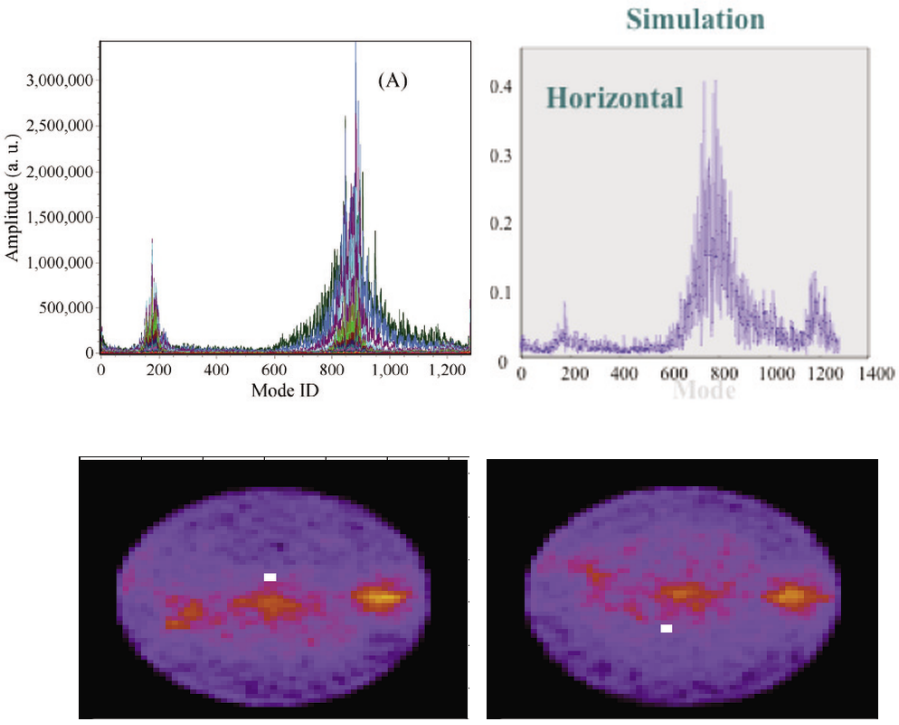

Fig. 17. (Color online) Top: Measured (left) and simulated (right) horizontal mode spectrum in KEKB. Bottom: Two snapshots of the simulated beam and e^- cloud motion. The white point indicates the beam passing through the chamber. Readapted from Ref. 76, thanks to K. Ohmi.

SEY of the Al arc beam chambers: electrons in bending magnets form stripes with a density that depends on the SEY, the stripes and the bunch train experience a coherent motion inducing the slowest unstable mode. This behavior is shown in Fig. 18 where the results of a tracking simulation are reported.

3.3. *Single bunch instability*

A beam going through an electron cloud focuses the electrons, so that the central density of electrons changes along the bunch. These pinched electrons induce nonlinear fields that can couple the motion of the head and tail of the bunch. As long as the bunch is perfectly centered on the pipe axis, the pinch also happens symmetrically and no coherent kick is generated along the bunch. If the head of the bunch is slightly displaced, an asymmetric pinch will take place, resulting into a net kick felt by the bunch tail. After several turns (passages through the electron cloud), the perturbation in the head motion transfers to the bunch tail, and its amplitude may grow and lead to an unstable coherent motion of the whole bunch. Depending on the cloud density,[3] the instability could appear as a beam breakup with a rise time much

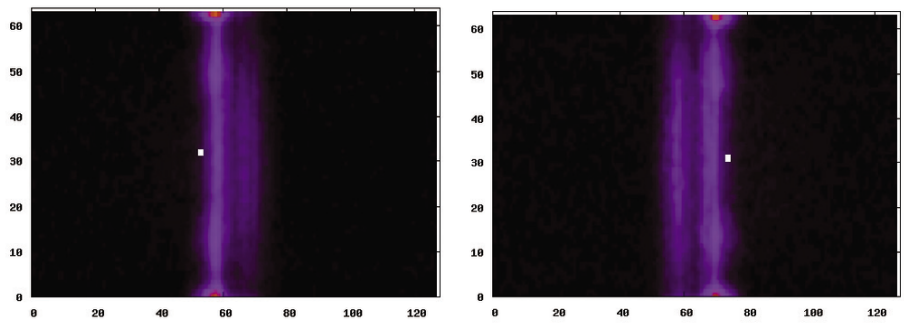

Fig. 18. (Color online) Two snapshots of the simulated beam and e^- cloud motion. The white point indicates the beam passing through the chamber. From Ref. 77, thanks to K. Ohmi.

shorter than the synchrotron period ($\tau \ll T_s$), as a transverse mode coupling instability with a rise time comparable to the synchrotron period ($\tau \approx T_s$), or as a conventional head–tail instability, which typically has a slower growth rate ($\tau \gg T_s$). In addition, the electron nonlinear fields induce a tune spread which may lead to resonance crossing resonance excitation and cause an incoherent emittance growth,[78–80] this mechanism can explain some beam observations at KEKB, SPS and LHC.

Reference 81 considered a two-particle model to explain a vertical beam-size blow up seen at KEKB by an electron-cloud driven head–tail instability. The derived formula for the instability threshold, in terms of critical electron density, is fairly accurate for short bunches (such as for KEKB or LHC). A fruitful approach to describe the electron cloud single bunch instability has been presented in Ref. 82, where the correspondence between the electron cloud wake and a conventional wake based on a damped broadband resonator model is established. In this approach, the wake function is expressed as:

$$W(z) \approx -c\frac{R_s}{Q_R}\frac{1}{\sqrt{1-1/(4Q_R^2)}}\exp\left(-\frac{\omega_R z}{2cQ_R}\right)\sin\left(-\frac{\omega_R z}{c}\right), \tag{19}$$

where Q_R, R_s and ω_s represent the quality factor, the shunt impedance and the frequency of the resonator. The resonator frequency is assumed to be roughly equal to the linear oscillation frequency of the electrons

$$\omega_R \approx \omega_e = c\left(\frac{2N_b r_e}{\sigma_y(\sigma_x+\sigma_y)\sqrt{2\pi}}\right)^{1/2}. \tag{20}$$

The advantage of this approach is that the classical theory of wake functions can be used to calculate the thresholds and growth rate of the different kinds of instability. In particular in Ref. 83 a very useful formula, valid in the limit of a coasting beam approximation, is given:

$$\rho_{e,th} = \frac{2\gamma\nu_s\omega_e\sigma_z/c}{KQ\sqrt{3}r_e\beta L}, \tag{21}$$

where K is a factor that takes into account the pinching of the electron cloud during the bunch passage. Although analytical models for the beam–electron interaction furnish scaling laws that can be used as independent benchmarks, computer simulations are indispensable for reliable predictions and understanding of the e^- cloud induced instability. Ordinary instability codes in use today model the interaction of an electron cloud with a single bunch on successive turns. The cloud is assumed to be generated by the preceding bunches and build-up simulation codes are used to obtain its transverse distribution. At every bunch passage through the cloud, the electron distribution is refreshed to its initial state. Typically, the beam-cloud interaction implemented in the simulation tools can be described as follow: both the beam and the electrons in the cloud are modeled as MP; the electrons are concentrated at one or several locations along the ring with an initial transverse distribution; the bunch is subdivided in slices which interacts with the cloud in sequence; beam particle are transported to the next interaction point along the ring by the use of appropriate transportation maps. The mutual interaction between beam and cloud MPs is described by the following equations:

$$\frac{d^2x_p}{ds^2} + K(s)x_p = \frac{r_e}{\gamma}\frac{\partial\phi_e(x_p)}{\partial x_p}\delta_P(s - s_e)\,, \tag{22}$$

$$\frac{d^2x_e}{dt^2} = \frac{e}{m_e}\frac{dx_e}{dt} \times \mathbf{B} - r_e c^2 \frac{\partial\phi(x_e)}{\partial x_e}\delta_P(t - t_p(s_e))\,, \tag{23}$$

where subscripts p and e identify beam particles and electrons respectively, $\mathbf{B}$ is an external magnetic field and both beam and electrons potentials $\phi_{e,p}x_{p,e}$ are solved using the PIC algorithm.[40] Based on this scheme, several instability codes, like PEHTS,[84] HEADTAIL,[85] MICROMAP[86] or CMAD[87] have been developed during the years in different laboratories to describe single bunch induced effects. Moreover, fully self-consistent codes such as like WARP-POSINST[88] or VORPAL,[89] which are able to compute the cloud generation over a bunch train around the ring as well as the resulting bunch instabilities, have been developed and are beginning to provide useful results. These codes have been benchmarked among each other and their predictions compared with experimental results. As an example,[90] results obtained with the codes HEADTAIL, CMAD, and WARP-POSINST have been compared using parameters corresponding to an LHC type proton beam in the SPS. This comparison is reported here in Fig. 19 showing the emittance evolution for different electron densities. It may be noticed that the results from CMAD deviate slightly for an electron density of $10^{13}e^-/m^3$, but overall there is a reasonable agreement between the three programs.

4. Surface Parameters

As we have previously seen, accelerator walls surface properties, like SEY, photon reflectivity, and PY do play a major role in governing electron cloud formation in accelerators. Of course, when certifying a material to be used as part of an accelerator, one has to choose it to meet a great number of properties (UHV compatibility,

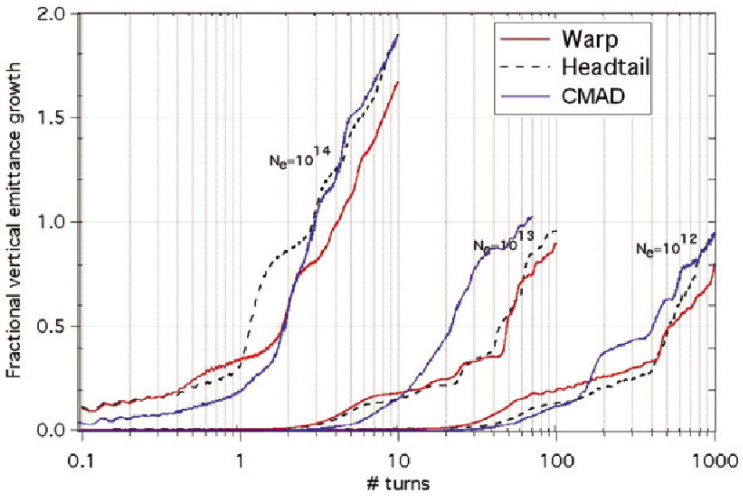

Fig. 19. Comparison of results from three simulation programs for a continuous focusing case for an LHC type beam in the SPS. From Ref. 90, thanks to M. Pivi.

magnetic permeability, mechanical properties, electrical conductivity, etc.). Those material properties will not be discussed here and can be found in reviews of accelerator vacuum and technology.[91–93] Here, we will concentrate on those material and surface properties which are essential ingredients in determining the e^- cloud formation.

4.1. *The secondary electron yield: Introduction*

SEY is an essential ingredient not only in connection to electron cloud issues but also since it influences material performance in many other field of research, like plasma physics,[94–96] space applications,[97–100] etc. Some of the results here presented are then taken from efforts done by a different community than accelerator scientists and will be of interest to a wider audience. Still, here we will concentrate mainly on materials connected to accelerator environment. For a more general discussion of SEY results on materials of interest in other research field, we will refer to existing literature.

In a simple approach, secondary electron-emission processes can be analyzed by a three-step process: penetration and absorption (or reflection) of the primary electrons (first step); transmission of the secondary electrons through the material (second step); and their final escape over the vacuum barrier (third step). The detailed analysis of each step has been discussed at length in many papers and reviews[104–108] and it is beyond the scope of our review. Briefly, the first two steps are governed by the universal mean free path curve reported in Fig. 20. If, in general, very low energy electrons like most of the secondaries have a significant

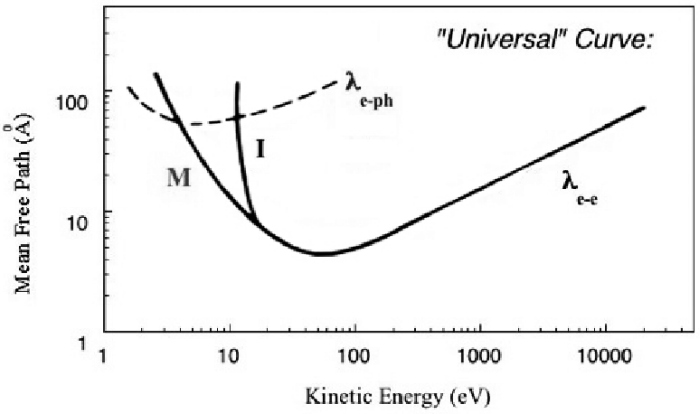

Fig. 20. The "universal" curve (mediated over a wide range of materials) of the energy dependence of the escape depth of electrons in metallic (M) and insulating (I) solids for electron–electron (λ_{e-e}), and electron–phonon ($\lambda_{e-\mathrm{ph}}$) scattering.[101–103]

ability to travel within the solid, impinging electron of energy between about 10 eV up to 1000 eV, travel, in the solid, only up to 10 Å (few monolayers) as it can be seen in Fig. 20. This very short mean free path for such impinging electrons contribute in determining the surface sensitivity of SEY. A primary electron with a reasonably high energy will not travel long before interacting with the solid and generating many internal secondary electrons. Secondary electron transmission strongly depends on the electronic properties of the material in which electrons travel and determines not only the SEY surface sensitivity but also its magnitude. In metals, any traveling electron loses its energy by interacting with conduction electrons, lattice vibrations, and defects. The intrinsic mechanisms through which secondary electrons lose their energy is so efficient that a sea of very low energy secondary electrons is quickly created. Once these electrons reach the vacuum barrier, only a small fraction of them have enough energy to escape into vacuum (third step). On the other hand, the wide band-gap present in insulators, prevents low energy secondary electrons from losing energy through electron–electron collisions. If the electron energy is below approximately twice the band-gap, the electron–phonon scattering ($\lambda_{e-\mathrm{ph}}$) is the dominating process, as schematically shown in Fig. 20. This results not only in a larger mean free path for SEY electrons (lower surface sensitivity) but also in a large SEY value, since the electrons reaching the vacuum barrier are more energetic than in metals and can overcome the vacuum barrier. To be noticed here that grain boundaries, defects and impurities present in technical materials can severely affect mean free path values, modifying electron–electron (λ_{e-e}), and electron–phonon scattering ($\lambda_{e-\mathrm{ph}}$). Any modification of the surface and near surface region affecting such scattering centers may indeed have a direct impact on the SEY.

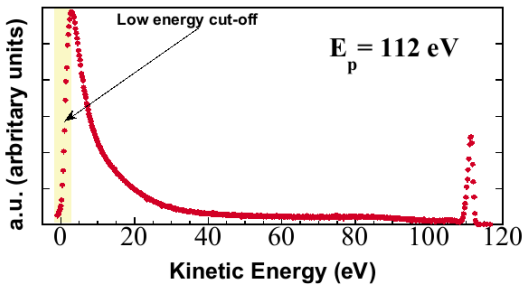

Fig. 21. Energy Distribution Curve (EDC) of the electrons produced by a 112 eV primary energy electron beam impinging on a Cu technical surface.[39] The cutoff at zero energy is mainly determined by the surface work function value.

The third step (escape of an internal electron into vacuum) is also essential to determine the actual SEY value. The kinetic energy of an internal secondary electron must be at least as big as W, so that an electron reaching the surface can escape. Actually, it also depends on the angle at which the electrons reach the surface. In fact, there is a limiting angle Θ_{lim} above which an electron having slightly more than enough energy to overcome the vacuum barrier, is anyway internally reflected by the surface.[109] The escape process introduces an additional dependence of the SEY on the outermost layer of the material under analysis since those layers can determine and influence the actual surface work function. It is well known that: (i) metal work function can vary due to different crystal surface orientation and reconstruction[110] (ii) sub-monolayer gas adsorption on metals can significantly vary their work function[111] (iii) metals with different surface roughness have different work functions.[112]

Any subtle change in W then corresponds to a significant variation in the number of electrons capable to escape from surface. This enhances the SEY sensitivity to surface conditions[113] and it can be better understood from Fig. 21, where a typical EDC of the electrons emitted from a Cu technical surface hit by a 112 eV primary energy electron beam is shown. At the same energy of the impinging electrons, there is the peak of the reflected electrons, here called $R_{\text{el}}(E)$ not to be confused with R which refers only to photon reflectivity, then a diffuse background representing electrons which suffered few energy losses and a high intensity of very low electrons, which are the so-called "true secondaries." As it can be clearly seen from Fig. 21, the number of very low energy electrons is increasing with a very high gradient up to a cutoff due to the material work function W. In simple terms, electrons that, outside the solid, have energy close to zero, inside the solid have the same energy $+W$. From Fig. 21, it is indeed clear that any subtle change in W, will allow (or stop) a very high number of electrons to be emitted from the solid, significantly influencing the measured SEY. To be noticed that, the width of the cutoff, shown in Fig. 21 is essentially connected to experimental aspects like the finite analyzer resolution and does not have any particular physical meaning.

Insulating materials are typically of little interest in this context, so no details will be given here, however it is important to keep in mind that surface contaminant layers, always present on real surfaces, may indeed have insulating properties, influencing not only the actual surface work function and the energy loss mechanisms governing the electron mean free path but also in general, most of the surface properties of a technical surface.

Before entering in the detailed analysis of SEY results, we think it is very useful to describe in some detail the experimental apparatus used to perform SEY measurements in dedicated laboratory. This is also due to the fact that some of the reported spread in literature results (specially for the SEY at very low energy) can be indeed ascribed to systematic errors.

4.2. *Experimental for SEY studies*

SEY ($\delta(E)$), is defined as the ratio of the number of electrons leaving the sample surface ($I_{\text{out}}(E)$) to the number of incident electrons ($I_p(E)$) per unit area. $I_{\text{out}}(E)$ is the number of electrons emitted from the surface but also the balance between the current flowing from the sample $I_s(E)$ minus the current impinging on the sample, $I_p(E)$, so that:

$$\delta(E) = I_{\text{out}}(E)/I_p(E) = (I_p(E) - I_s(E))/I_p(E) = 1 - I_s(E)/I_p(E)\,. \qquad (24)$$

To measure SEY we have different experimental schemes: one can separately measure the impinging electron current generated by the electron source $I_p(E)$ by means of a "Faraday cup," and then measure the sample current $I_s(E)$ as done, for example, in Refs. 18, 19, 39, 114–117; one can simultaneously measure $I_s(E)$ and $I_{\text{out}}(E)$, collected either from a cage around the gun and placed in front of the sample as shown in Fig. 22 and done, for example in Refs. 15, 118–124 or using an hemispherical collector all around the system.[104,125–130] All methods have been used and, with some care, produce very similar results.

To avoid modifications due to electron bombardment, as discussed in Sec. 5.5, it is preferred to work with low currents in the experimental determination of SEY which imply the usage low noise cables and stable nano-Amperometers. Also, most of the experiments are performed at normal incidence.

When dealing with electrons, especially at very low energy (ideally ≈ 0 eV), it is essential to limit spurious effects caused by residual electromagnetic fields, which will alter the electron trajectories as a function of their energy. Some of the setup used to measured SEY do not take any particular caution to control such spurious effect and indeed, the presence, for instance, of the earth magnetic field, and, in some cases, the stray field of ion pumps mounted on the vacuum system, do affect SEY accuracy, especially at very low energy. Other setups use either Helmotz coils[131] to zero (up to some nT) magnetic field at the sample position, or μ-metal chambers, constructed by using a nickel-iron alloy (75% Ni, 15% Fe, plus Cu and Mo), having a very high magnetic permeability. This reduce to less than 0.3 μT any

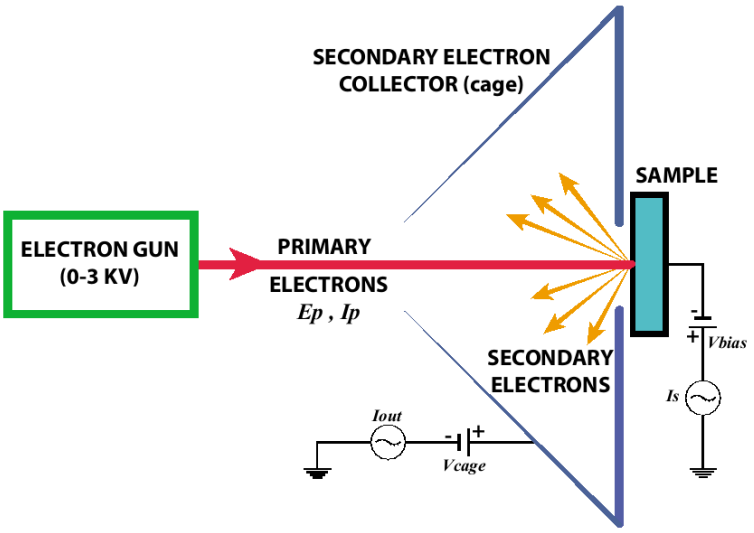

Fig. 22. SEY experimental apparatus in use at CERN.[15,118–124] Readapted from N. Hilleret.

magnetic field within the vacuum system. Those remedies allow experimentalists to confidently measure SEY up to a low impinging electron energy of about few eV. One more technical consideration derives from the fact that no electron source gives reliable flux at very low energy, and that space charge effects tends to spread up very low electron beams (with energy lower than $\sim$10–20 eV).[129] For this reason, the gun should be placed as close as possible to the sample in order to minimize the beam path, and the $\sim$0 eV energy electron beam landing on the sample is best obtained by slowing down the impinging electron energy by the retarding negative (few tens of volts) bias voltage. This allow to work using the e^- gun operating at energies always higher than $\sim$20–50 eV, that is, in a region where they are stable and produce a well collimated beam. Ideally, the beam should just see the retarding voltage symmetrically acting from the sample, and extreme care should be taken since any asymmetric electrostatic component could deviate the impinging beam (as a function of its energy) and give rise to spurious effects specially at very low landing energies. One further common requirement for the experimental apparata measuring SEY is the capability of operating in Ultra High Vacuum, UHV (base pressure $\leqq 2 \times 10^{-10}$ mbar), not only because UHV is necessary to operate electron guns and because these pressures are representative of those of any accelerator complex (which is what we want to simulate) but also in order not to modify the analyzed surface by spuriously adsorbed gas contaminants. In fact, as it has already been discussed in the previous section, SEY is intrinsically a highly surface sensitive technique and the surface composition plays an essential role in determining it. To keep the base pressure as low as possible, UHV systems needs to be equipped

with adequate pumping and be baked-out at about 100–150°C. State of the art SEY experimental systems are normally equipped with a fast entry lock to insert samples into the baked system in UHV conditions, without spoiling its vacuum. Sample fast entry-lock allows not only pumping and bake-out time to be saved, but also avoid undesired sample thermal treatments, which would occur during sample-system bake out, most probably modifying the SEY values. Different e^- guns are then used to perform the experiments. If some setups use home made e^- guns, with marginal capability of beam focusing, a number of products fulfilling most of the SEY experiments requirements are available from the market. Well focused, or collimated low to medium current electron guns, typically needed for Low Energy Electron Diffraction (LEED), Electron Energy Loss Spectroscopy (EELS), etc. have been developed in the surface science community. Such high performance guns are routinely used for SEY experiments delivering typical e^- currents ranging between tens of μA down to a fraction of nA, 10–5000 eV primary energy, and in a small (less than a 0.3 mm^2) and stable (both in current and position) beam spot on the sample. Since the sample is biased, the gun should operate at energies higher than the bias (normally ranging from 20 to 70 eV) and with a typical sample to gun distance of less than 30 mm, to minimize beam perturbations due to any residual electromagnetic field. Most of the experiments tend to use as small as possible impinging electron current (few nA or less), compatible with current meters noise. This is done to limit the known SEY variations during data acquisition. Such effect, called "scrubbing"[118,132] has been recently thoroughly studied and its chemical origin has been identified.[114,115] This will be discussed in Sec. 5.5, being one of the most powerful mitigation mechanism adopted so far.

Once the e-gun produces the desired beam, one needs to measure precisely its intensity and shape as a function of e^- energy and a "Faraday cup" is typically used. In most setups, the Faraday cups are home made instruments designed to measure all the current entering in a hole (or slot). In Fig. 23, we show the Faraday cup used in Refs. 18, 19, 39, 114–117.

This home made Faraday cup, consists of three gold coated insulated plates closely spaced (about 1 mm); the first one has slots and it is grounded, the second one, has also slots and can be placed at a bias voltage or grounded as well and the third one is the collector plate biased at a positive voltage of about 75 eV. The second plate is designed to send back to the collector those electrons which are emitted at energies higher than the bias voltage. This electron detector can be inserted and removed from the e^- beam path, by a motorized linear mechanism with a precision better than 10 μm. When the beam enters one of the slots, the measured current can be used to derive the beam profile (at least in the direction perpendicular to the slot) as a function of the beam position within the slot and the background outside the main electron spot. This is a very important tool to optimize the e^- gun operating parameters for SEY experiments, since the desired beam should have a known diameter (preferentially small) and a very low halo not to have electrons impinging on the sample and not counted by the Faraday cup. The

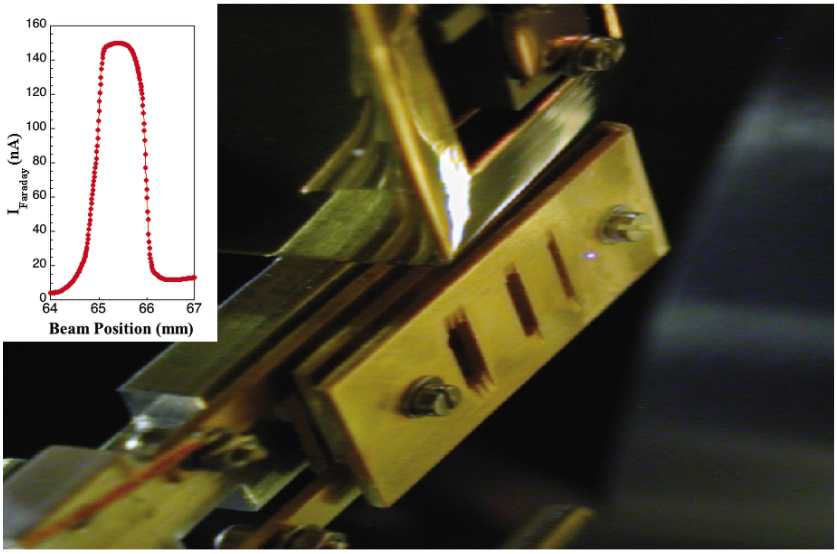

Fig. 23. (Color online) Image of the Faraday cup used to measure $I_p(E)$ in different experiments.[18,19,39,114,115] In the picture, we can also see differently wide slots $(1, 2, 3$ mm) which can be driven into the beam to measure beam profile and background. A blue spot on the right side of the 1 mm slot is the actual electron beam (at 500 eV) hitting a fluorescent powder previously deposited on that external part of the Faraday cup. The inset shows an x scan of the Faraday cup through the 1 mm slot.

inset shows the current measured from the Faraday collector ($I_{\text{Faraday}} = I_p$) during an x-position scan allowing the beam to pass through the 1 mm slot. The computer controlled motorized x-scan allowed us to set the electron gun parameters to have a well focussed beam ($\leqq 0.2$ mm in diameter) with a marginal intensity outside the main spot, and a flat intensity across the slot. Such electron beam spot can be visually observed looking at the blue spot close to the 1 mm slot in Fig. 23. This spot is the image of a well focussed 500 eV electron beam hitting a fluorescent powder previously deposited on the external part of the Faraday cup. The use of such powders are extremely helpful to visually determine the beam spot size, but works only for electron beam of energy above few hundreds of eV. For the determination of the spot profile of lower energy beams, the Faraday x-scan is then essential.

To measure $I_p(E)$, some experimentalists use to directly apply a positive bias to the sample. This method of measuring the impinging electron current introduces a systematic error (function of the energy of the beam and of the positive bias value used) since one loses (and does noncount) all the electrons escaping from the sample used as a e^- collector, with energy higher than the bias. An example of this is shown in Fig. 24 where we compare $I_p(E)$ as measured with the Faraday cup shown in Fig. 23 or by applying a positive bias of 75 eV on the Cu sample.

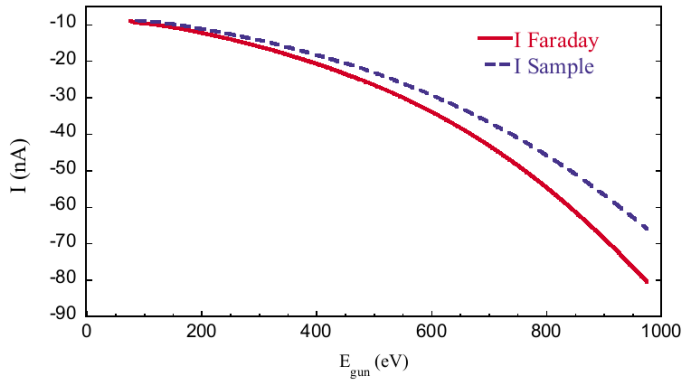

Fig. 24. (Color online) Comparison between $I_p(E)$ as measured with a Faraday cup (red curve) and by applying a positive bias of 75 eV on the sample (blue curve).

The data shows that, for the bias used, the experimental error on the estimated current increase with energy, it is nearly 10% at 500 eV, and then increase constantly. Measuring $I_p(E)$ without using an *ad hoc* Faraday cup would affect the measured SEY by a systematic error that can invalidate the accuracy of such experiments.

Figure 25 shows a typical SEY curve measured from the as received polycrystalline Cu surface representative for the one used in the LHC beam screen shown in Fig. 2. For the purpose of identifying significant parameters to compare different SEY curves, one can single out: (a) a low energy region (0 eV $\leq E_p \leq$ 20 eV); (b) the energy value at which the $\delta(E)$ reaches its maximum: $\delta_{\max}(E_{\max})$. If most

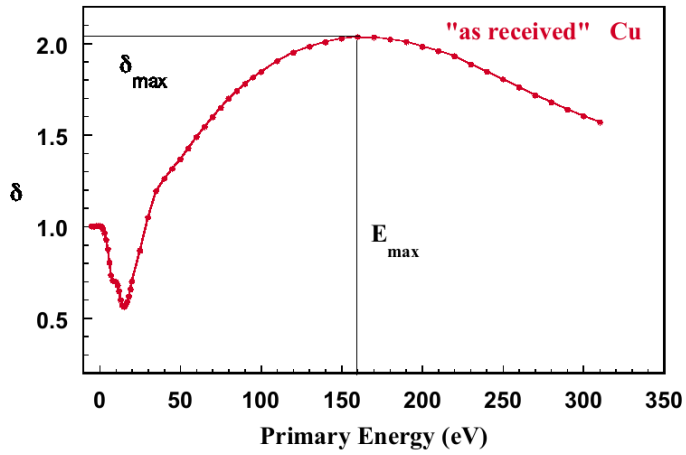

Fig. 25. Typical SEY curve measured from an "as received" polycrystalline Cu surface representative for the one used in the LHC beam screen (data from Ref. 39).

of the following discussion will deal with the $\delta_{\max}(E_{\max})$ of each surface, we stress here that for e^- cloud related studies, $\delta_{\max}(E_{\max})$ is indeed a relevant parameter, but it is the full dependence of SEY on the impinging primary energy which does play an essential role in determining e^- cloud related effects in accelerators.

4.3. *Secondary electron yield of technical surfaces*

As it has been clearly shown previously, e^- cloud in accelerators strongly depend on SEY value from accelerator walls. Such walls are normally metals (Al, Cu, Stainless Steel (St St)) or metal coated (with TiN, TiZrV, a-C, etc.) surfaces which are all technical surfaces, whose SEY can be only marginally related to the SEY of the corresponding clean metal. This is because the discussed strong surface dependence of SEY implies that the, although thin, surface contamination layer, when present, may affect the SEY value much more than the metallic material underneath. For this reason we concentrate only on selected technical materials leaving the analysis of SEY from clean metal surfaces to other dedicated reviews.[104–108,133] We will also compare each technical surface with its atomically clean counterpart. This will put into evidence the role played by surface contaminants in determining the actual surface SEY.

Many SEY studies have been performed in the accelerator community since SEY has been recognized to be one of the most important surface parameter for e^- cloud related studies.[134–139]

Most of such studies do also analyze SEY stability and its modification during operation and e^- cloud build-up. Here, we will briefly report results on such "as received" surfaces leaving the detailed analysis of how they modify their SEY upon electron bombardment when analyzing the surface behaviors upon "scrubbing" in Sec. 5 when discussing mitigation strategies.

We report in Fig. 26 the SEY curves from "as received" technical surfaces as measured in Ref. 118. Apart from the striking high value of the Al technical sample, mainly due to the insulating Aluminum-Oxide surface layer,[116,117] we see that Cu, Ti and St St show very similar SEY curves and that only TiN shows an "as received" SEY lower value, at least in the presented data set.[118] Other works on "as received" TiN[22] technical surfaces actually show a SEY very similar to the one of Cu and St St, showing that more than by the different substrates, the SEY value of an "as received" surface seems to be determined by the existence of a very similar contaminant layer, common to most surfaces (but Aluminum, which tends to oxidize in air much more promptly than the other surfaces here presented). In Table 2, we report some of the $\delta_{\max}$ values reported in recent studies on the most common materials in use for accelerator vacuum chambers. Selected references, when available, are given in the fourth column. For completeness, when data were missing, as for some sputtered clean surfaces, data have been collected on purpose for this review. The similarity of most of the data and the spread in the reported values, most probably due to subtle differences in bulk but also in contaminant compositions, roughness,

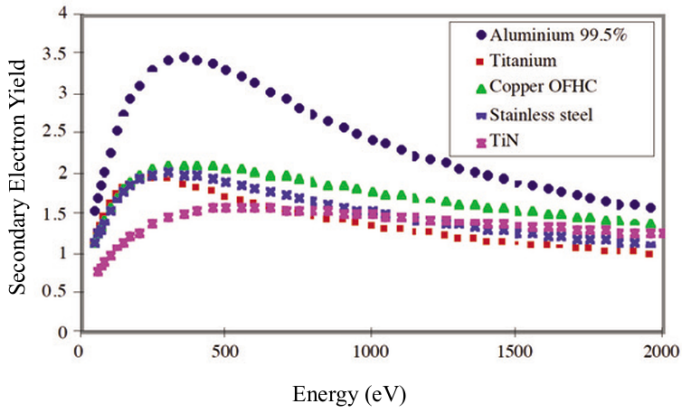

Fig. 26. Typical SEY curves measured from various "as received" technical surfaces of use in accelerators. From Ref. 118, thanks to V. Baglin.

Table 2. SEY of technical samples used in accelerators and of their atomically clean surfaces.

Material	δ_{max}	E_{max} (eV)	References
Cu "as received"	1.9–2.2	150–220	39, 118, 121
Cu "Ar^+ sputtered"	1.4	350	115
Al "as received"	3.3–3.8	200–300	116–118
Al "Ar^+ sputtered"	1.0	250	118
St St "as received"	2.2–2.5	200–300	118, 133, 141
St St "Ar^+ sputtered"	1.4	280	133 and this review
TiN "as received"	2.3–2.5	200–300	22 and this review
TiN "Ar^+ sputtered"	1.3	320	133 and this review
TiZrV "as received"	2.0–2.2	200–300	22, 119
TiZrV "activated"	1.0–1.2	200–300	22, 119, 123, 142, 143
a-C "as received"	0.95–1.8	200–300	124, 141, 143
Clean HOPG	0.95–1.05	280–350	114, 124, 141

etc. seems to indicate that a database containing SEY values of such materials is not particularly useful, and no attempt will be made here in this direction. This is confirmed by looking at the δ_{max} values reported in Table 2, once the technical surface under study has been atomically cleaned by "in vacuum Ar^+ Sputtering" as done for Cu, Al, TiN and St St, or thermally cleaned as done for TiZrV and Highly Ordered Pyrolytic Graphite (HOPG). In most cases, the atomic cleanliness of the analyzed surfaces has been confirmed by XPS analysis. The polycrystalline clean surface δ_{max} does then depend on the chemical composition of the bulk (and clean surface) material, but has little or no relation to the corresponding "as received" values confirming how dominant is the contamination to determine a common "as received" δ_{max} value.

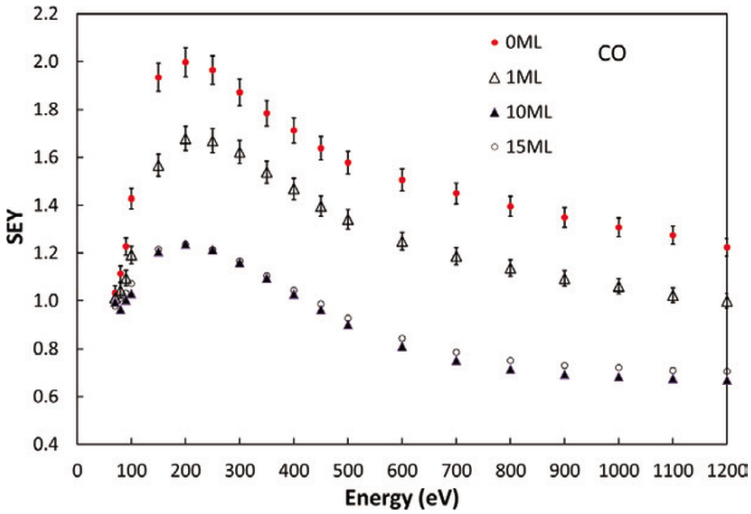

Fig. 27. SEY of adsorbed CO on "as received" Cu at 4.7 K as a function of primary energy for different coverages. From Ref. 140 thanks to M. Taborelli.

A very interesting result is shown in Fig. 27, where we report SEY as measured on a copper surface held at 4.7 K as a function of increasing CO coverage.[140] Already a single CO ML physisorbed on the Cu cold surface significantly modifies its SEY and additional CO deposition results in a completely different SEY value of about 1.2. This result is not only very important to confirm the extreme surface sensitivity of SEY but suggests that, when discussing SEY of cold surfaces (like for the LHC dipoles) great care must be taken in considering any eventual surface modification induced by gas physisorption.

4.4. *Low energy SEY*

The behavior of SEY at very low impinging electron energy need to be discussed separately since, although of paramount importance in many applications, is still under debate. Such energy region of the SEY spectrum plays a major role in determining the performances of many scientific systems and devices. In recent years, a series of publications[18,19,39] on a detailed study of SEY from Cu technical surfaces presented new observation reporting, for the first time, the tendency of SEY not only to reach 1 as E_p approaches 0 eV, but also to stay significantly above 0 for quite an extended energy region, having a minimum SEY of about 0.5–0.7 at E_p as high as 10–20 eV. Such a typical behavior can be seen in Fig. 25. This low energy behavior was clearly stated to be relative to the actual technical Cu surface studied and a strong warning was given against the extrapolation of such results as being a general property of SEY. More recently, Kaganovich and others,[144] put this observation into question suggesting instead that the measured SEY is somehow due

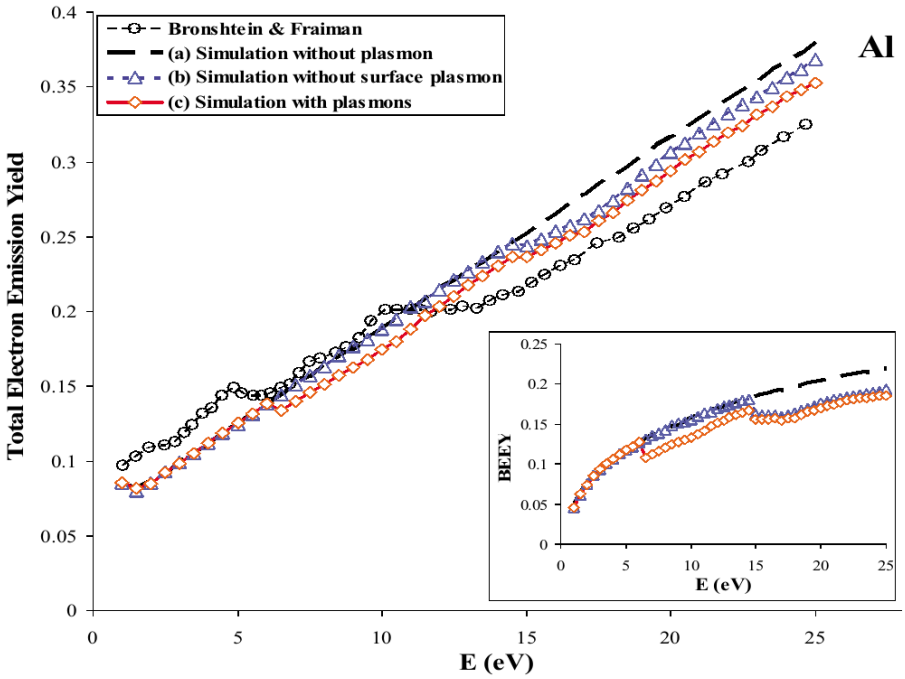

Fig. 28. Simulated SEY in three cases: (a) without plasmon, (b) with volume plasmons but without surface plasmon, (c) with volume and surface plasmons; compared with the experimental SEY of Bronshtein and Fraiman.[145] The inset represents the backscattered electron emission yield (BEEY) simulated in the three cases. From Ref. 109, thanks to J. Roupie.

to experimental artifacts, since the SEY value at zero impinging energy is and must be zero or close to zero and the SEY curve should nearly monotonically decrease to this value. The authors corroborate such statement with experimental findings taken from the literature.[125,145–149] Also, some theoretical computations predict a very low SEY at low E_p tending to zero at zero impinging energy. Figure 28 shows a very good agreement between simulated SEY and experimental data from Ref. 145 for the case of atomically clean Al.

In those simulations, the effect of surface-barrier potential which causes the reflection of incident electrons was also taken into account. The reflected electron coefficient R_{el} remains low even at 1 eV ($R_{\mathrm{el}} \approx 0.04$), as seen in the inset of Fig. 28, in perfect agreement with experimental results published a few decades ago by Heil and Hollweg.[148]

On the other end, a recent work by Cazaux,[150] while discussing, with a different approach, some theoretical and instrumental issues concerning electrons impinging on a solid surface with $E_p < 10$ eV, produce simulations which are consistent with an increasing R_{el} (up to $R_{\mathrm{el}} = 1$ for $E_p \approx 0$ eV) and with a significantly nonzero SEY for E_p below 10–20 eV. An example of such simulations is shown in Fig. 29.

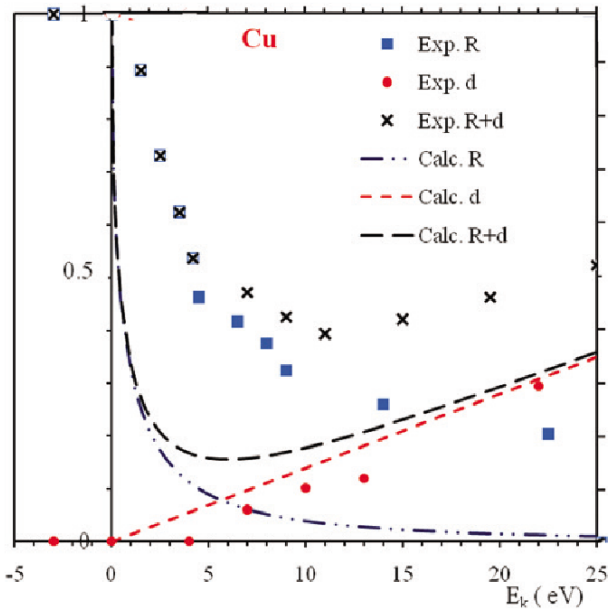

Fig. 29. Comparison between the experimental results[18,19,39] (symbols) and the calculations in Ref. 150 (lines). From Ref. 150, thanks to J. Cazaux.

The simulations performed by Cazaux are more than consistent with the data presented and discussed in Refs. 18, 19 and 39 and supports not only that electron reflectivity R_{el} at zero landing electron energy can be expected to be close to 100% but also that SEY value at low impinging energies (from zero to some tens of eV) has values significantly higher than zero.

On the experimental side, it is clear that the measurements at very low energies are very difficult since it is an intrinsically difficult region to be investigated,[109,129,130] and that, especially at E_p very close to zero, space charge, electromagnetic fields, beam energy resolution, etc. may act on the very low energy electron beam potentially affecting any detailed experimental SEY determination. Still, most of the various systems used for SEY experiments are indeed capable of reproducing the low energy behavior reported in Refs. 109, 125, 145–149 for clean metals, while on technical surfaces, like the LHC Cu used in Refs. 18, 19 and 39, such behavior is never reproduced, and a significant SEY is measured. Belhaj and coworkers,[130] observed that SEY is and stays higher than 0.6 for energies as low as 3 eV for a series of different surfaces exposed to atmosphere, as shown in Fig. 30. Even if their spectra start at 3 eV, confirming the inherent difficulties to confidently measure SEY at even lower impinging electron energy, those data, shown in Fig. 25, corroborate the observation presented in Refs. 18, 19 and 39 and confirm the suggested importance of surface contamination in determining the SEY behavior at

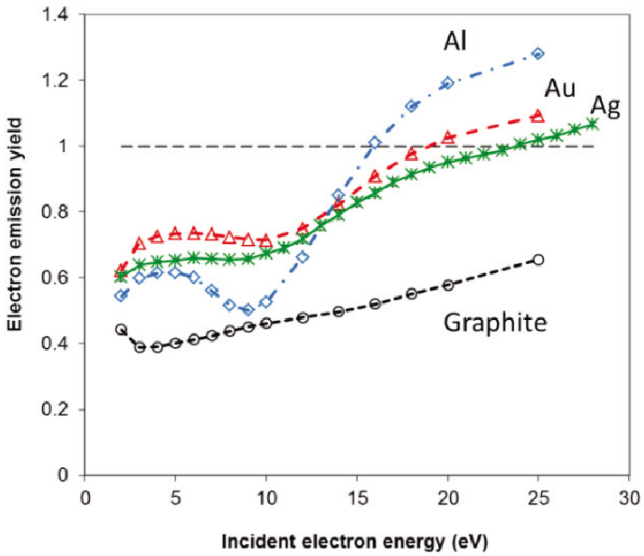

Fig. 30. Total electron emission yield of technical materials (Aluminium, Gold, Silver and Graphite). It should be noticed that all the samples were exposed to ambient atmosphere for a long time. From Ref. 130, thanks to M. Belhaj.

very low impinging energy. As here shortly discussed, the behavior of SEY in the very low energy region is far from being fully understood and experimentally investigated, and its technological importance is expected to push towards a more precise understanding in the near future.

4.5. *Photoelectron yield*

PY, also known as quantum efficiency (QE), measures the number of electrons produced, through the photoelectric effect, per incident photon as a function of its angle of incidence and energy. The photoelectric effect is a very well-known effect: Heinrich Hertz in 1887[151] discovered that electrodes illuminated with ultraviolet light create electric sparks more easily. In 1905, Albert Einstein[152] discovered the law of the photoelectric effect and was therefore awarded the Nobel Prize in 1921. Photoemission is based on this effect and represents a very powerful tool which has been developed and is widely used to study electronic properties of matter.[153,154] Despite an extremely wide literature on photoemission and related studies on a immense material variety, very little use of such literature can be done in e^- cloud related context since very little studies have been done so far on technical surfaces. Moreover, most if not all photoemission experiments study the difference in structure, lines and line shapes present in the spectra whereas no attention is paid to the normalized (to the photon flux) intensity of the signal, which is the parameter of interest here.

As it has been discussed in the previous sections, PY from industrial surfaces is an essential ingredient in e^- cloud formation. Electron cloud related resonant phenomena are not the only detrimental effects occurring in accelerators and originated by the background electrons. Ohmi and Zimmermann,[81] in 2000, when attempting to explain the observed vertical beam-size blow up for KEKB, introduced the concept of single beam instability threshold suggesting that the mere existence of a certain electron density in the accelerator (for the KEKB case around 7×10^{11} $e^- m^{-3}$) is able to detrimentally affect the beam quality as discussed in Sec. 3. Hence, the electron density has to be carefully simulated, and PY and R experimentally measured to correctly feed the necessary simulations.

First attempts to study, in detail such properties from technical samples has been pioneered, in the nineties, irradiating beampipe samples with the whole SR spectrum produced in the dipoles of available accelerators (EPA at CERN and VEPP2M at BINP).[155,156] With such setups a change in the photon energy spectrum could be only obtained by modifying, whenever possible, the electron beam energy, resulting in a quite complex procedure. Later, such topic was tackled by using SR dedicated beamlines at available facilities.[16] With this dedicated setup one could study not only the measured PY from the proposed materials, prepared on an industrial scale, but also the energy and, in some cases, the angular dependence of the emitted electrons when the sample is excited with either a WL spectrum, simulating that one in the arcs of the LHC at nominal parameters, or monochromatic light in the 10 to 200 eV photon energy range. PY of different "as-received" samples illuminated by a WL SR spectrum mimicking the one in the arcs of the LHC at nominal parameters ($E_c = 44$ eV) is shown in Fig. 31. These data[16] have been taken with the light incident at 45°, which is far from representing the grazing angle of incidence at which light impinges in real machines. For this reason, they should be considered with some caution and more experiments, done in more realistic geometrical conditions, should be performed.

A series of new experiments in this direction is just starting and interesting new results, obtained in geometries close to the ones of interest have been presented at the last ECLOUD meeting in 2012.[157,158] In Fig. 32, we report PY data from a Cu technical surface of LHC beam screen, as a function of photon energy at different incidence angles. As a general trend, we clearly observe the increase of the photon yield for increasing photon energy, which is expected considering that more energetic photons have more energy to donate to the low energy electrons which mainly contribute to the total PY. From Fig. 32, we also note that, for all photon energies, the PY increases at decreasing incident angles. This can be attributed to the reduced photon penetration at very grazing angles, so that more electrons are produced by the photoelectric effect closer to the surface, which are ready to escape into vacuum. Of course, in order to generate numbers to be fed in the e^- cloud simulations, one should measure PY from a WL spectrum similar to the one emitted by the machine under analysis. This needs further investigation and will be most hopefully pursued in the near future. Of course, using monochromatic light,

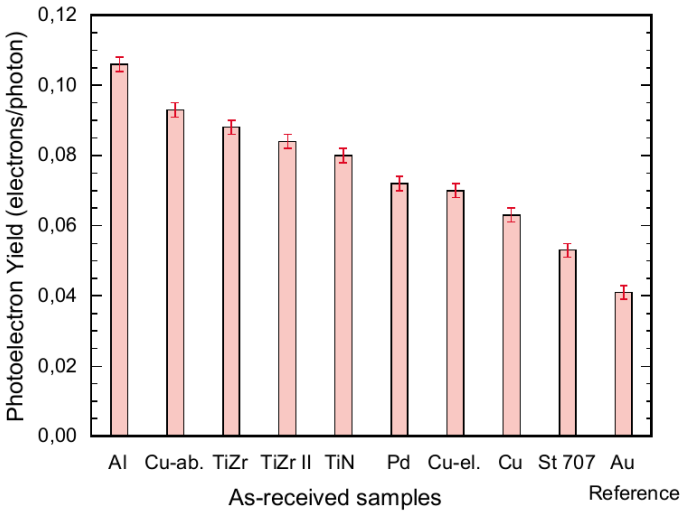

Fig. 31. PY of different "as-received" samples illuminated by a WL SR spectrum mimicking the one in the arcs of the LHC at nominal parameters ($E_c = 44$ eV). The data,[16] which are sorted in descending order, have been taken with light incident at 45°.

one can try to reconstruct WL PY, but also extract additional information on the chemical nature of the sample under analysis. As can be seen in Fig. 32, the PY curves measured with increased photon energy are essentially proportional to the sample absorption structure, which is not a smooth structure, but have singularities at absorption edges. Such edge structures are indeed observable in Fig. 32. Next to the Cu L-absorption lines (Cu L-edge around 933 eV), the surface contaminating layer is observed. Both C and O are visible at their atomic absorption edges

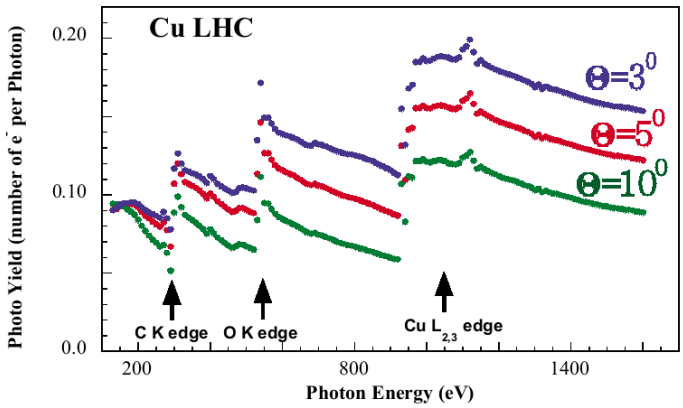

Fig. 32. PY from a Cu technical surface of LHC beam screen, as function of photon energy at different incidence angles.[157]

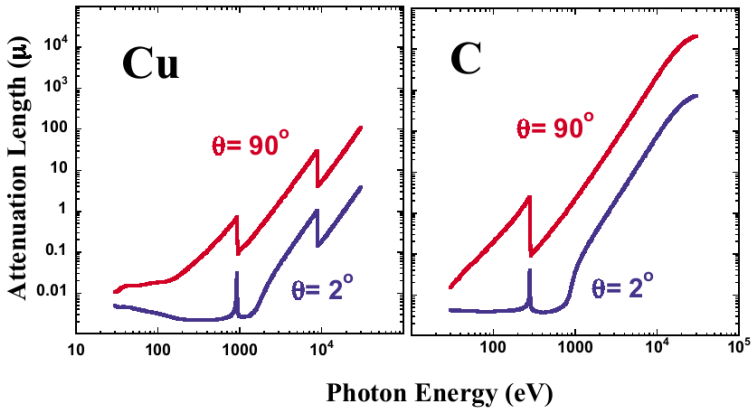

Fig. 33. Calculated energy dependence of the photon attenuation length for Cu and C at 90° and 2° angle of incidence. The attenuation length is the depth into the material, measured along the surface normal, where the intensity of X-rays falls to $1/e$ of its value at the surface. Calculations were performed using the Henke tables[160] available on the web.[162]

(C, O K-edges at around 284 eV and 543 eV). Detailed analysis of such resonance regions around the absorption edges would yield further information on the chemical composition of the coatings and interfaces, and on the individual thicknesses. For instance, it will be possible to characterize what chemical compound determines the PY, its eventual modification by photon irradiation and compare it to what has been recently studied on electron irradiated Cu.[114]

An interesting aspect, which is evident in Fig. 32 is that at incidence angle around 10° or more, the PY measured with a monochromatic photon of around 150 eV is very similar to the PY measured with a 1500 eV photon. The PY at 1500 eV slightly rises in comparison to the PY at 150 eV but is always less than a factor 2 despite the obvious fact that a 10 times higher energy photon will produce within the solid a much higher number of electrons potentially contributing to the total PY. Such experimental evidence, reported in Fig. 32 can be explained by the energy-dependent cross-sections of the impinging photons. Such energy dependence, which is of course material-dependent, is shown in Fig. 33, where the attenuation length in Carbon and Copper is calculated as a function of photon energy and angle of incidence.[159,160] The attenuation depth is defined as the depth into the material along the surface normal where the intensity of X-rays falls to $1/e$ of its value at the surface. From such calculation, it is evident that the ability of a photon to travel within a solid greatly increases (the photoelectric cross-section decrease[159,161]) with its energy. PY is determined by the number of electrons produced within the solid that can escape from the surface and, since the electron mean free path (shown in Fig. 20) is quite small, it is clear that only photoelectrons produced close to the surface will be able to escape into vacuum, contributing to the PY signal. So that, the more a photon penetrates, the less it produces photoelectrons that can be

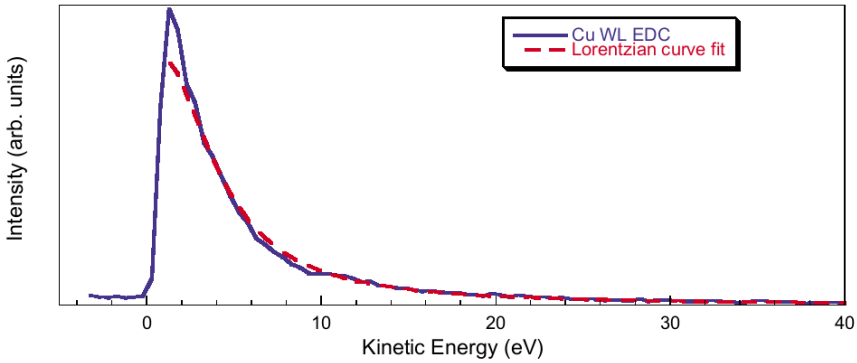

Fig. 34. (Color online) Energy Distribution curve (EDC) as excited by White Light (WL) SR mimicking that in the arcs of the LHC at nominal parameters ($E_c = 44$ eV), for an "as received" Cu sample from LHC beam screen. The red curve represents a Lorentzian fit to such Cu WL EDC.[16]

emitted into vacuum. These is only partially compensated by the higher number of electrons produced by a higher energy photon. This simple reasoning and the calculations done at various angle of incidence shown in Fig. 33, also explain why the more grazing incidence photons have an higher PY. In fact, they will travel more closely to the surface and produce, in this region, more electrons which can escape and contribute to PY. These qualitative arguments gives an important hint for further studies: the most important photons to study for PY productions are the ones with low-medium energy (roughly in the region between few eV, i.e. above W, and up to less than a KeV) and impinging at very grazing incidence.

One more parameter used in e^- cloud simulations which is related to PY but is more complex than a single value, is the actual energy distribution of the photo-emitted electrons by WL irradiation. Such EDC has been rarely studied, and one of the few results obtained in this context is reported in Fig. 34, where the WL EDC for the Cu sample is shown.[16] The most appropriate description of the energy distribution in this case was found to be Lorentzian in nature centered at 0.64 eV and with a width of 3.7 eV. Unfortunately similar experiments performed on different materials and surface conditions show that it is not possible to describe the photoelectron distributions of different materials with similar Lorentzians scaled to their PY intensities. In each separate case, experimental input is required to obtain the realistic electron distribution to be used in the simulations.

PY parameters are also relevant to study the importance of the e^- cloud activity as a possible heat source in the superconducting undulators operating in SR facilities like the Advanced Photon Source (APS), at Argonne National Laboratory. Harkay *et al.*[158] to better understand the primary electron generation in the APS used a beamline at the Australian Light Source SR facility to characterize samples of the Al APS vacuum chamber. The total PY, referred as Quantum efficiency (QE) in Ref. 158, and the photoemission spectra were measured as a function of surface

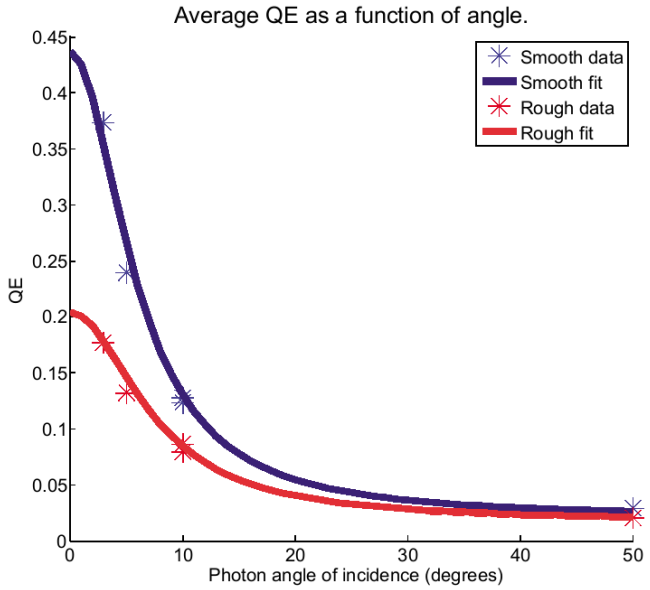

Fig. 35. The average Quantum efficiency (QE) plotted as a function of photon angle of incidence for Al samples with different roughness. Higher photon angles of incidence have a smaller QE than lower angles of incidence and the higher roughness decreases the measured PY. From Ref. 158, thanks to K. Harkay.

roughness, sample temperature, incident photon energy, and incident photon angle. The PY dependence on incident photon energy and angle are consistent with literature results;[16,157] little if any difference have been observed on PY when varying sample temperature from 300 to 180 K, and an expected but interesting variation of the measured PY was clearly observed on samples with different roughnesses. This is shown in Fig. 35, where a higher average PY is measured on a polished Al sample, confirming that, also for the PY, the detailed morphology of the analyzed sample surface may play a significant role.

4.6. *Photon reflectivity* (*R*)

In connection with PY, there is a renewed interest to estimate the energy and the distribution of photon absorption sites, which are not only critical inputs to codes which model the growth of electron clouds but also of relevance to the analysis of electron induced single bunch instabilities as discussed in Sec. 3. This interest prompted a serious effort to track SR photons generated in storage rings and linacs. One of the most complete tracking tools[68,163] has been recently developed as part of the Cesr-TA program,[68,164] and includes scattering from the vacuum chamber walls, based on the X-ray data from an LBNL database for the smooth-surface reflectivity, together with an analytical model[165,166] for diffuse scattering from a surface with

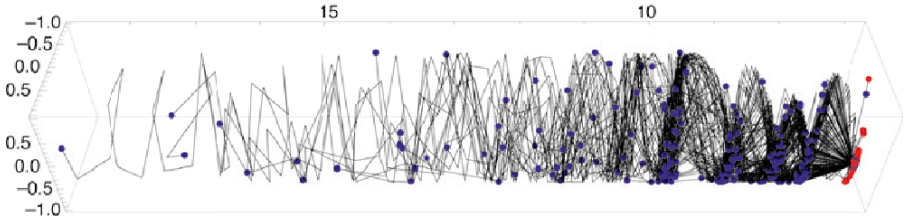

Fig. 36. (Color online) Photon trajectories from a dipole in three dimensions. The photon source is on the right. Black lines are trajectories, and blue dots are photon absorption sites. The transverse geometry has been distorted from an ellipse to a circle, and the longitudinal dimension has been rectified and divided by 10, for purposes of illustration. From Ref. 68, thanks to G. Dugan.

finite roughness. Such program, called Synrad3D can handle any planar lattice and a wide variety of vacuum chamber profiles. One result of such a powerful tool is shown in Fig. 36, where the photon trajectories from a dipole are calculated.

Such simulation codes requires validation and an experimental campaign has been launched to measure realistic R from industrial surfaces with the rugosity values typical of the real accelerator walls. Such experiments can be performed as a function of photon angle of incidence, reflection and photon energy by using existing experimental setups developed in SR facilities to experimentally analyze the reflectivity from quasi-perfect optical elements, multilayers, etc. Preliminary studies have been done at Elettra[17] in Trieste, where the saw-tooth solution adopted to reduce photon reflectivity on the top and bottom surfaces of the LHC dipole has been validated and reflectivity quantified, as shown in Fig. 37.

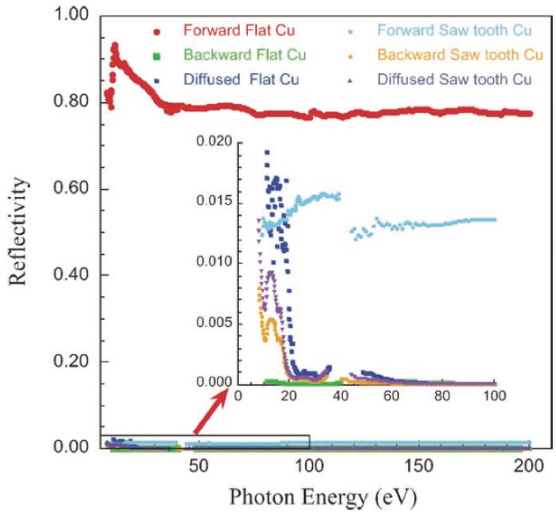

Fig. 37. Reflectivity of the measured flat and saw-tooth Cu surfaces versus impinging monochromatic photon energy between 8 and 200 eV (from Ref. 17).

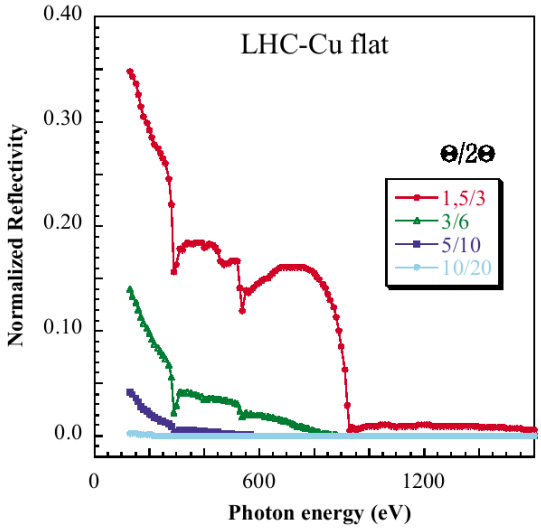

Fig. 38. Reflectivity of a LHC-Cu sample representative of the flat part of the beam screen, as a function of photon energy for various incidence angles Θ and emission angles 2 Θ.[157]

An *ad hoc* setup, present at BESSY II (SR facility in Berlin) under the scientific supervision of F. Schäfers, has been more recently used for preliminary studies[157] on Cu surfaces representative of LHC beam screen present in the dipoles. In Fig. 38, the reflectivity of such samples is shown as a function of the photon energy for selected incidence angles. The investigated energy range presented here is between 130 eV and 1600 eV. We also observe in such monochromatic reflectivity experiments, resonance structures due to absorption of the Carbon and Oxygen contaminated surface layers (C, O K-edges at 284.4 eV and 543.1 eV) and of Cu (Cu $L3$-edge at 932.7 eV). As expected, reflectivity is higher at lower grazing angle incidence and at low photon energy. These data confirm the importance of studying photo reflectivity in geometries as close to the one actually occurring in accelerators.

5. Countermeasures

Due to the discussed importance to have a stable low SEY and, in some cases, low PY surface, a number of mitigation strategies have been analyzed and pursued. Still, there is not a unique and final solution able to solve all problems related to an high SEY, and while Research and development (R&D) is still actively ongoing, different mitigation strategies, or a combination of them, have been adopted so far and will be discussed here shortly. Generally countermeasures implemented today are of two kinds: passive countermeasures, which aims to the reduction of the surface parameters such as SEY and/or PY, and active countermeasures which introduce external electric or magnetic fields in order to reduce the e^- cloud formation.

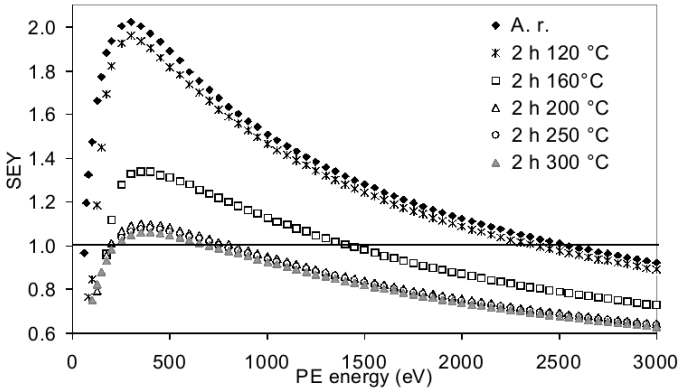

Fig. 39. SEY versus primary electron energy (PE) of the TiZrV NEG coating; as received (Ar) and after 2 h heating at 120°C, 160°C, 200°C, 250°C, 300°C. Data from Ref. 119, courtesy of M. Taborelli.

5.1. *Coatings*

Of course the ideal solution to solve most of the e^- cloud related instabilities would be the identification of a material with intrinsically low and stable SEY, being compatible with all vacuum and impedance requirements. Such research has not yet given the desired results, in particular because, as discussed in Sec. 4.3, every material interacts with atmosphere and get contaminated by it. This unavoidable surface contamination layer renders most coatings unstable during operation and with higher than required SEY, and must be used in combination with other countermeasures. We want here to underline though, that there are two relevant exceptions to this reasoning, namely TiZV NEG coating and a-C. In case of TiZrV NEG coatings, developed at CERN by Benvenuti as diffuse pumps,[142] a mild thermal annealing in UHV (activation) is shown to remove most of the surface contaminants,[22,119,123,142,167] resulting in a stable and close to atomically clean surface with $\delta_{\max}$ about 1.1. This can be seen in Fig. 39, where the SEY is measured as a function of annealing at different temperatures. Also, some observations done at the European Synchrotron Radiation Facility (ESRF) indicates that impedance budget issues can be kept under control[168] as most of the problems related to the coating itself, like pealing-off, etc. Indeed, if UHV is required and if space allows to externally heat the accelerator wall at around 200 °C to activate the NEG film, such coatings are a very efficient e^- cloud mitigator, as shown by the behavior of all the NEG coated warm section of LHC.

At CERN, the need to have intrinsically low SEY (PY) surfaces in regions like the LHC and SPS magnets, where the required thermal treatments could not be conceived nor implemented, triggered the research of alternative solutions. It has been found[124,141,169] that a-C can be grown and maintained in particular conditions to be significantly free from surface contaminant due to the very low reactivity of

such surface to atmosphere, resulting in an intrinsically low SEY material with $\delta_{\max}$ about 1. Such deposition procedure are now mature to produce such films on industrial scale[169] so that a-C represent nowadays a potentially very interesting solution to mitigate ECE.

Clearly, also such coatings risk to loose their e^- cloud mitigation properties if contaminants are physisorbed on their surface, so that extra care has to be taken to maintain as clean as possible such low SEY coatings.

5.2. *Solenoid field*

Using solenoid magnets to sweep an electron cloud has been known and discussed since the design stage of the B factory.[170] A longitudinal solenoid field B_s may confine the electrons near the wall of the vacuum chamber where they are created and therefore may reduce the cloud density near the beam. This has been analyzed in details by simulations[171] confirming that, even a weak longitudinal solenoid field forces the mainly low energy ($\approx$ 5 eV) electrons of the cloud into circular orbits that hit the chamber surface after performing about half a period. Hence, if this process is fast enough, the solenoid field can clear the electrons between two bunch passages. In fact, also in presence of the bunch potential, electrons still perform circle-like orbits and are maintained close to the chamber's wall. Large energy gains are avoided (ideally, below E1 in Fig. 7) and thus the SEY of the electron-wall collision is reduced, resulting in an effective mitigation of the multipacting effect.

A clear example of the mitigation potentiality of a weak solenoid field in reducing detrimental effects on accelerator performance is shown in Fig. 40 where the e^- cloud induced pressure rise in the LHC merged vacuum is shown. As soon as both contra rotating beams are injected with a given intensity, a clear pressure rise is observed in two sectors of the merged vacuum namely A4L1 and A4R1. Such pressure rise is unexplainable without assuming e^- cloud formation, and as it stands, is a very explicative example on the detrimental effect that e^- cloud formation can have on beam vacuum. As soon as a solenoid field is switched on (first in one than in both sectors), the pressure essentially recovers, showing how solenoids fields can reduce ECE.

Going more in details, for a relativistic electron, the equation of motion can be written

$$\dot{\vec{v}} = -\vec{v} \times \frac{e\vec{B}}{\gamma mc} = \vec{\omega} \times \vec{v}\,, \tag{25}$$

where $\vec{\omega} = e\vec{B}/(\gamma mc)$ is the cyclotron frequency of the electron. The solution of (25) is a helix parallel to B_s with radius $r = v_\perp/\omega$. Hence it can be easily verified that for typical values a small solenoid field (10–100 G) is enough to keep the electrons close enough to the beam chamber. A resonance occurs when half a period equals the interval between two consecutive bunches[173]

$$\frac{T}{2} = \frac{s_b}{c}\,. \tag{26}$$

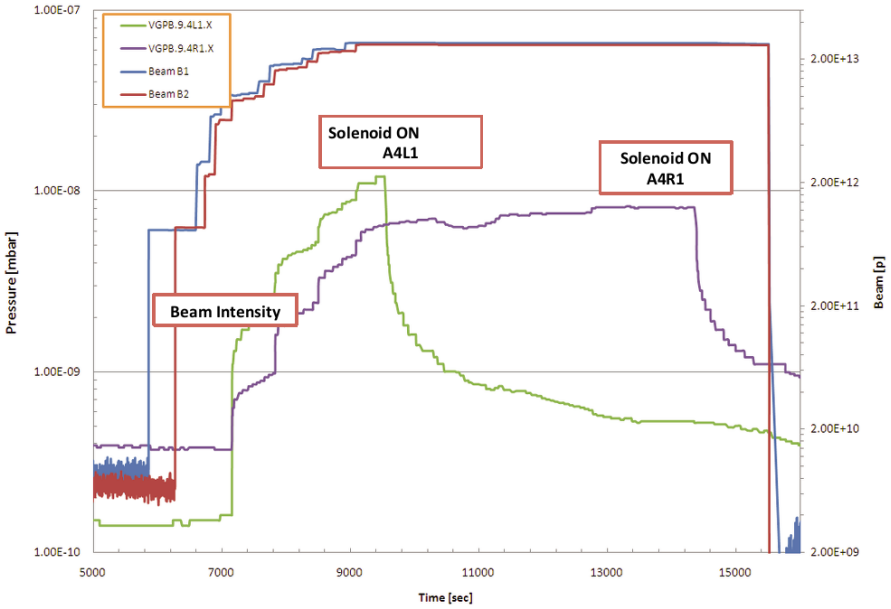

Fig. 40. First evidence of the effect of a solenoidal field on the measured merged vacuum for LHC at 450 GeV, 150 ns bunch spacing. From Ref. 172, thanks to V. Baglin.

For a solenoid field B_s, the cyclotron period is

$$T_c = \frac{2\pi m_e}{eB_s}\,, \tag{27}$$

where m_e is the electron mass and e is the absolute value of the electron charge. Combining Eqs. (26) and (27), the resonant magnetic field is given by

$$B_{\rm res} = \frac{\pi m_e c}{s_b e}\,. \tag{28}$$

If this occurs, electrons hit the chamber wall in synchronism with the bunch passage and multipacting is enhanced. However there is a threshold value of bunch population, related to the energy gain of the electrons in the cloud during the passage of a bunch and independent of the bunch spacing,[173] above which the resonance takes place. As shown in Fig. 41, simulations for DAΦNE exhibit a threshold $N_b = 5 \times 10^{10}$ for both single and double bunch spacing.[72]

Solenoids cannot be adopted in many parts of the ring not only where space constraints do not allow to wrap any coil around the chamber but also because in magnetic field regions, external solenoid fields are not effective in suppressing the build-up of the electron cloud. This make solenoids an effective countermeasure but not sufficient to guarantee total suppression of ECE.

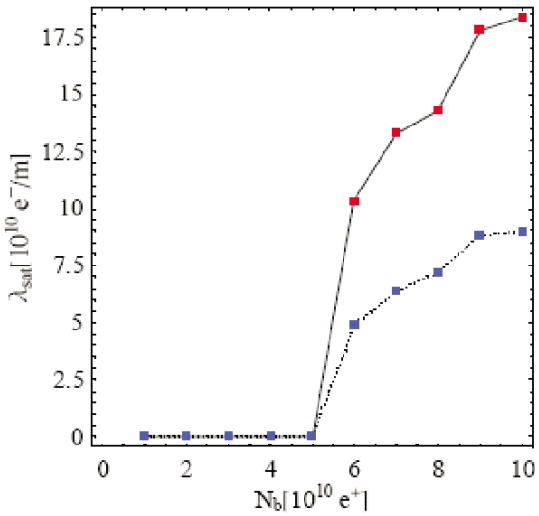

Fig. 41. (Color online) Saturated density as a function of the bunch population. Red dots represent the case of Lsep spacing and 66 G field. Blue dots represent 2 Lsep spacing and 33 G field (from Ref. 72).

5.3. *Electrodes*

A complementary and very efficient additional mitigation solution is the use, where possible, of electrodes. This is because in bending magnets the electrons of the cloud can easily drift in the vertical direction from one side of the chamber's surface to the other side under the force of a clearing field. For short bunches, the build-up of the electron cloud depends on the multibunch multipacting. Therefore, the clearing effects depend on the spacing of the bunches. The requirement for the clearing electrode is to clear the electrons within one bunch spacing. For long bunches, electron cloud multipacting is a single-bunch phenomenon in which strong multipacting occurs at the tail of the bunch. Because of the beam's space-charge effect, clearing the electrons is more complicated than for short bunches. Electrons generated by gas ionization are trapped inside the coasting beam and can cause transverse instabilities. The clearing field pulls the electrons out from the beam's potential well. The first experiences with e^- cloud clearing have been acquired with short button-type electrodes.[174] To cover longer sections, a proposed solution with rather low impedance and good mechanical properties consists of resistive layers deposited onto a ceramic or an enamel strip inside the beam pipe. Recently, such test electrodes have been successfully installed and tested in single wiggler magnet section of the existing machines CERN PS,[175] CESR,[176] KEKB.[177,178]

In the DAΦNE collider, another type of electrode never adopted before has been proposed and installed;[179] moreover, this device, shown in Fig. 42, has been installed in all positron ring arcs allowing a detailed measurement campaign. Figure 43

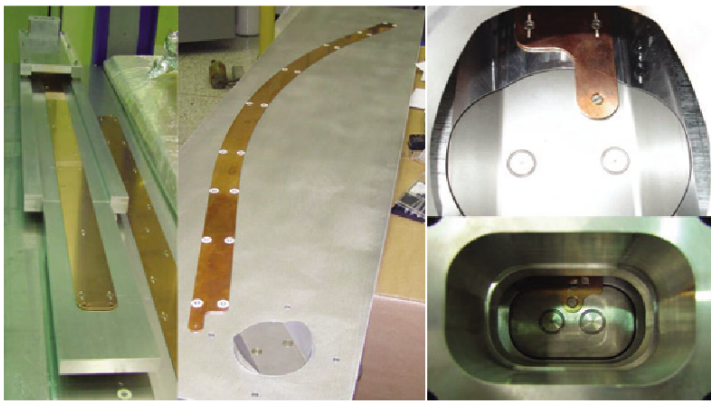

Fig. 42. Images of the electrodes inserted in the wiggler (left) and dipole (center) chambers of the DAΦne positron ring and details of the electrodes output connections (right) used in Ref. 179.

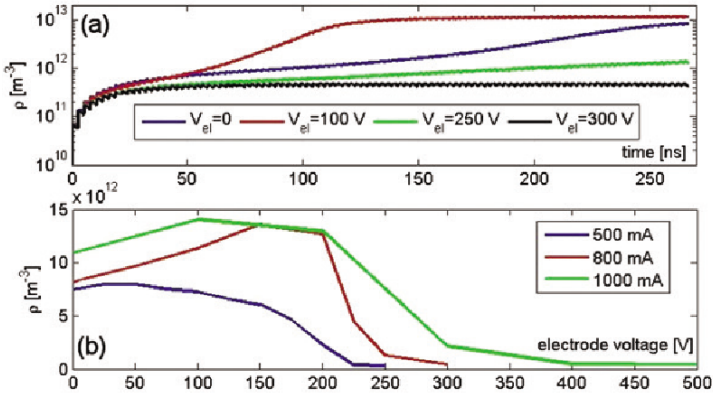

Fig. 43. (a) Evolution of the averaged cloud density for different values of the electrode voltage. (b) e^- cloud density at the end of the bunch train. Parameters used in the simulation are the primary electron rate 0.008, photon reflectivity 100% (uniform), maximum SEY 1.9, energy at maximum SEY 250 eV, vertical magnetic field 1.64 T, bunch length 12.3 mm, bunch hor./vert. size 1:08 mm = 0:05 mm, and hor./vert. chamber sizes 12 cm/2 cm (from Ref. 179).

shows the e^- cloud density evolution for different values of the electrode voltage for 800 mA in 100 consecutive bunches as computed with the code ECLOUD. A non-monotonic dependence of the saturation density on the electrode voltage is clearly observed. In particular, the maximum value is reached around 150 V. For higher voltages, the density sharply decreases. We see that already at 300 V, it is reduced by about 2 orders of magnitude. The same behavior is observed for different values of the beam current, as shown in Fig. 43. Such a behavior was attributed to the fact that the electrodes accelerate the electrons of the cloud and, since the SEY has its maximum at the energy of 200–300 eV, we can expect some e^- cloud density

increase due to the secondary electrons from the electrode surface at voltages of 200–300 V. Clearly the e^- cloud dynamics is complicated by the beam electric potential and the e^- cloud space charge effect, but the experimental results provide a good chance for the numeric code benchmarking. Of course electrodes may induce impedance problems, which should be carefully considered before adopting electrodes to mitigate ECE. In most accelerators, it could not be easy to find space to accommodate them without significant extra cost. A nontrivial technical problem is to guarantee electrons insulation during operation and avoid accumulation of dust.

5.4. *Geometrical modification*

The idea behind any geometrical reduction of SEY, is simply based on the experimental fact that electrons contributing to SEY have an energy distribution peaked at very low kinetic energy (as shown in Fig. 21 and discussed in Sec. 4) and an angular distribution with its maximum at normal emission and a significant decrease at grazing angles. So, if only electrons emitted from the surface at grazing incidence "see" the beam, and the ones emitted at normal incidence are shadowed by the surface itself, than a net reduction in SEY is expected. Pioneering work[180–184] has been performed and different types of grooves have been theoretically analyzed and then their SEY has been measured. We show in Fig. 44, two types of grooved surfaces which have been produced and studied in recent years: triangular and rectangular grooves. The first ones are characterized by the angle α between continuous triangles, while the rectangular ones are characterized by the period b, dwell width a, depth h and a flat top thickness. We can understand the expected SEY reduction considering an initial electron hitting the surface at point A: such electron produces secondaries, as shown in Fig. 44. Depending on the emission angle, some of the secondaries can escape the groove and move away from the surface. Other secondaries will hit an inner side of the groove. With some probability they will be absorbed, or they can generate further secondaries. The process may repeat several times and the net SEY measure will show a reduced value from the one measured from the flat surface. The presence of a magnetic field will enhance the SEY reduction due to the additional spinning of the emitted electrons along the field lines within the grooves.

Panels (c) and (d) in Fig. 44 show the actual results as measured in Ref. 184 experimentally confirming the actual SEY reduction obtained from a grooved surface. Of course, costs estimates, impedance budget, etc. must be carefully considered and evaluated before adopting such otherwise very efficient mitigation schemes.

In line with this research, recent studies have considered the creation of geometrical modification at a micro- or sub-micron scale by chemical etching.[185,186] Such promising research line will need substantial effort not only to reproducibly manufacture such additional roughness but to carefully study its effect on impedance, conductivity and all the required properties of such a low SEY-PY surface.

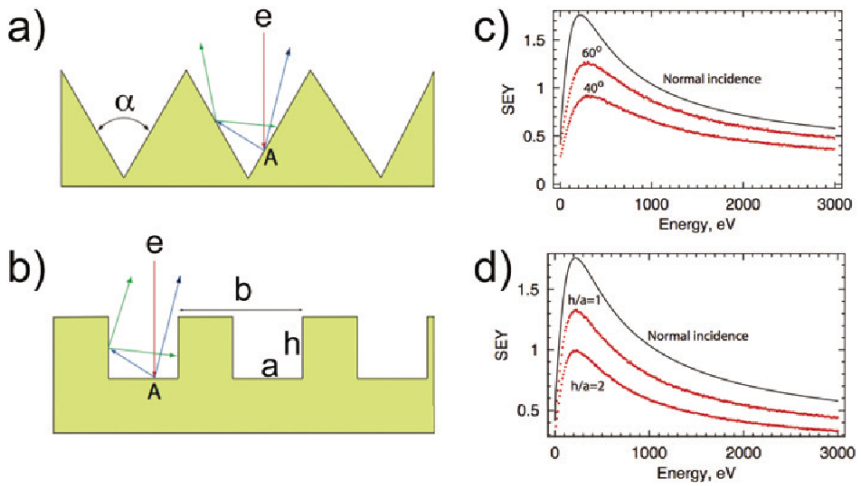

Fig. 44. (Color online) Triangular (a) and rectangular (b) grooves on the surface. Triangular grooves are characterized by the angle α. Rectangular grooves have a period b, width a and depth h. (c) Comparison of the effective SEY for $\alpha = 60°$ and $40°$ triangular grooves and the reference case of the flat surface and (d) SEY for rectangular grooves assuming $a = 2/3b$. Red dotted lines correspond to different aspect ratios of the rectangular grooves: the bottom line is for $h/a = 2$ and the middle one corresponds to $h/a = 1$. Full line corresponds to the reference case of the flat surface. From Ref. 184, thanks to M. T. F. Pivi.

5.5. *Electron and photon scrubbing*

As said in Sec. 4.3 and shown in Fig. 26, most if not all materials used in accelerator technology have a significantly high SEY, much higher than needed to avoid e^- cloud related instabilities. Pioneering work done at CERN in this context,[118,120,122,167,187] observes that when a surface is exposed to an electron beam, its SEY decreases. This is shown in Fig. 45, where the SEY values of a Cu technical surface after subsequent electron doses are reported. Such observation had and still has profound impact for cloud related mitigation studies for the simple reason that electron bombardment is what is actually happening during e^- cloud formation. It appears that, while the cloud is forming, it is able to cure its detrimental effects: the electron beam hits the accelerator walls and causes a reduction of their SEY value. Such process, called "Scrubbing," shows a kind of self-mitigation mechanism first proposed in the late nineties[15,188] and then adopted[134–136] as the base line design to cope with any detrimental effects of e^- cloud related instabilities in LHC. Such strategy has been shown to be a winning one, since LHC could run, at 50 ns, allowing the discovery of the Higgs boson, and to perform many other successful experiments[189–192] without suffering any detrimental effect from e^- cloud formation. Clearly, only the future operation of LHC at 25 ns and full beam current will confirm its complete validity and further studies are needed to validate such mitigation strategy for LHC upgrades and/or other machines.

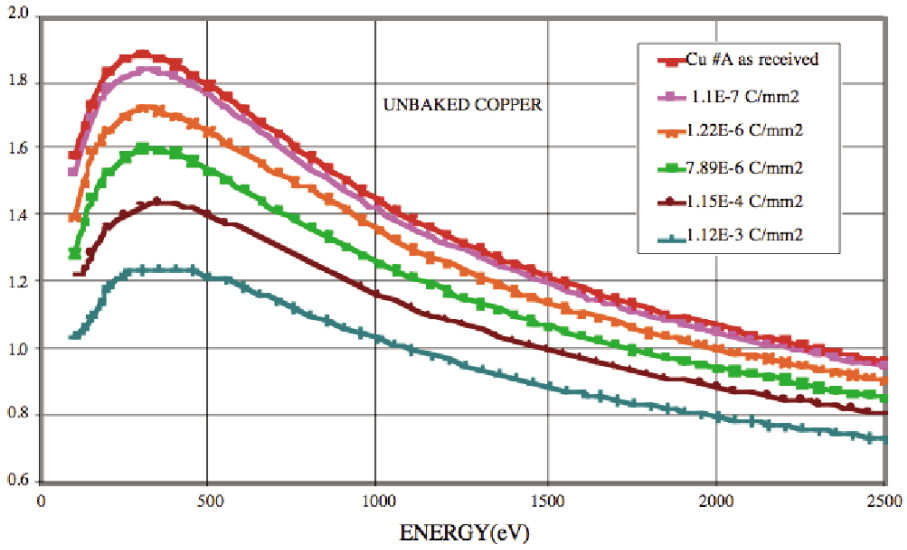

Fig. 45. Variation of the SEY of copper with incident electron dose. From Ref. 118, thanks to V. Baglin.

The laboratory observation at the base of such mitigation solution, shows a drastic reduction of the initially high SEY ($\delta_{\max} = 1.9$–2.1) of the Cu surface seeing the beam in the cryogenic dipoles, to a much lower value ($\delta_{\max} \sim 1.1$) after a certain electron dose. This is shown in Fig. 45 where a series of SEY curves have been measured after different irradiation doses.[118] In Fig. 46, $\delta_{\max}$ versus dose is shown[120] and indicates that an electron dose between 8×10^{-4} Cmm^{-2} and 2×10^{-3} Cmm^{-2} is necessary to reach a $\delta_{\max}$ lower than 1.3. The minimum of the $\delta_{\max}$ (close to 1.1) is obtained for an electron dose of about 1×10^{-2} Cmm^{-2} corresponding to the so-called "fully scrubbed" surface. Most if not all of the laboratory data confirming such evidence[19,39,118,120,122,134–137,187,193] are taken as a function of the electron bombarding dose, as shown in Fig. 46, while the dependence on the energy of the impinging electrons was never studied and was typically chosen to be around 500 eV or more. The underlaying assumption that scrubbing depends only on the electron dose and not on the energy of the impinging electrons, has been recently questioned,[114,115] and will be discussed in the following, together with the detailed chemical origin at the base of the scrubbing process.

As already said, the decision to base LHC mitigation strategy on scrubbing has now showed its validity, but at first, has caused some interesting scientific debate. In fact, not only other experiments, like the one performed at SLAC laboratory,[194] obtained similar trends but with significantly different initial and final $\delta_{\max}$ values during scrubbing, but also there was no clear understanding of its physical origin. This aspect was clearly stated in the conclusion of Ref. 120: "*Although the*

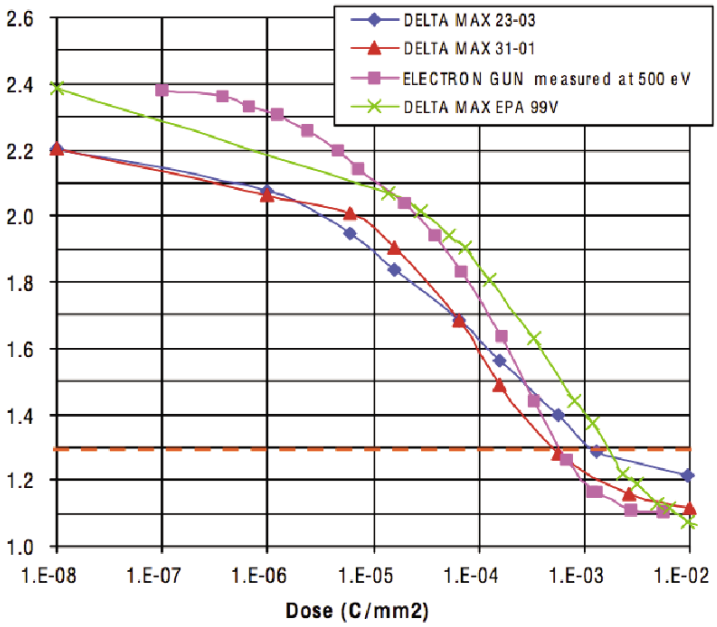

Fig. 46. The variation of δ_{max} for Cu as a function of the incident electron dose and as obtained with different experimental setups and dosing procedures (see Ref. 120 for details). From Ref. 120, thanks to V. Baglin.

phenomenon of conditioning has been obtained reproducibly on many samples, in different experimental setups, the exact mechanism leading to this effect is not properly understood. This is of course not a comfortable situation as the LHC operation at nominal intensity relies on this effect. Further studies are going on to try to elucidate the main physical parameters responsible for this beneficial effect." and triggered a series of experiments[114–117,195–197] aiming to the detailed comprehension of the chemical variations induced by electron irradiation on technical surfaces. Some of those studies have demonstrated that the beneficial effect of electron beam scrubbing on these surfaces coincides with the formation of a graphitic surface film.[114,195,197] Since the SEY of graphite and, in general, of carbon based materials is lower than that of air exposed metals, the presence of the a-C thin film reduces the effective SEY of the surface.[124] Graphitic film growth occurs because, in general, technical surfaces are covered by C containing contaminants that, once exposed to the electron flux, tend to decompose and partly rearrange in graphitic assemblies.[196,198] The occurrence of material transformation at the atomic level induced by electron irradiation has been often reported in the case of thin films and nanostructures.[199,200] The experimental evidence for this phenomenon is shown in Fig. 47, where SEY and X-ray photoelectron spectroscopy (XPS) measurements of a Cu prototype of the beam screen adopted for LHC are reported.

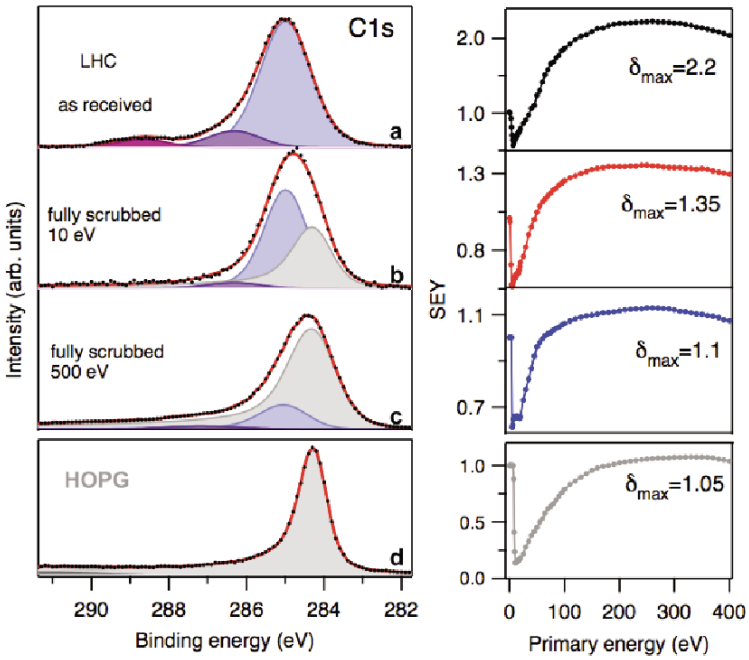

Fig. 47. C1s XPS spectra (left panel) and SEY curves (right panel) measured on the LHC Cu sample: (a) "as received"; (b) after a dose of 3×10^{-2} Cmm^{-2} at 10 eV; (c) after a dose of 3×10^{-2} Cmm^{-2} at 500 eV; (d) on a freshly cleaved HOPG surface.[114]

The most striking changes occurring at the surface, as seen by XPS, are exhibited by the C1s core level spectra reported in Fig. 47 (left panel), together with the relative SEY curves (right panel), for the three representative cases: (a) the "as received" surface, and the surface fully scrubbed at (b) 500 eV and (c) 10 eV. The bottom panels of Fig. 47 shows, for comparison, the C1s core level spectrum measured on a freshly cleaved HOPG, together with its SEY curve. Without entering into the details of the spectral analysis, performed by standard core level deconvolution, one observes that in the "as received" sample the C1s spectrum can be decomposed into a main peak, to be attributed to sp^3 hybridized C atoms in C–C[201] and C–H bonds[202] and two weak components at 286.3 and 288.6 eV ascribed to single or double C–O bonds.[203] Electron beam irradiation decompose the weakly bound species and converts the sp^3 hybridized C atoms into a network having predominantly sp^2 bonds, as shown by the appearance of the graphitic component in the C1s spectrum.[201] The chemical modification observed are directly connected to the SEY reduction reported in the right panel of Fig. 47. While electrons irradiation at 500 eV modifies the chemical state of almost all the contaminating C atoms producing a graphitic-like layer coating the copper surface, in agreement with previous literature results,[195,197] we notice how the C1s spectra taken after a dose of

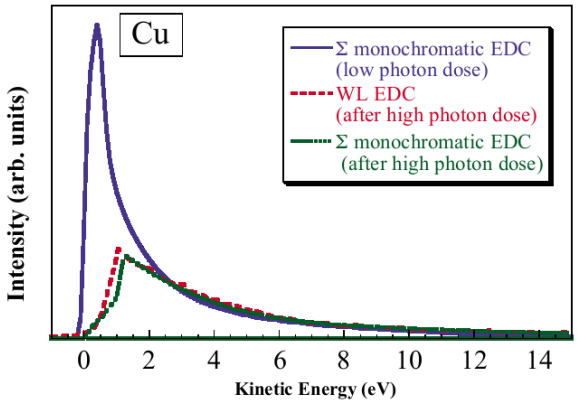

Fig. 48. (Color online) Low photon dose EDC spectrum from a Cu sample (blue solid line) compared with its corresponding WL EDC (red dashed and green line) (see Ref. 16 for details).

3×10^{-2} Cmm^{-2} at 10 eV (curve *b*) in Fig. 47, reveal a limited sp^3–sp^2 conversion and a consequently limited scrubbing efficiency for low energy beam, reaching a stable final SEY value of $\delta_{\max} = 1.35$. This suggests that the decrease in SEY depends significantly on the kinetic energy of the primary electrons.[114,115] Such dependence, its chemical origin and the relevance of such observation on the commissioning scenario for the LHC, (where the energy of the electrons in the cloud is expected to be low, see Fig. 12) need further consideration and will trigger further studies in years to come.

Important to mention is that analogue SEY reduction (and energy dependence) has also been observed when bombarding several "as received" substrates of different nature like TiN and St St. The C1s spectra, taken in similar conditions as those described in the case of Cu, do show nearly identical behavior in terms of the increase of the component attributed to the sp^2 bonds and SEY reduction. This general trend shows, as far as we know, at least one relevant exception represented by Al alloy used in some accelerators like PETRA3 in Hamburg and DAΦNE in Frascati. Upon scrubbing of Al alloy samples, carbon graphitization does not take place, most probably due to the exceptional reactivity to oxygen of the Al alloy surface as the one used in PETRA3.[116,117] Also photon irradiation has been observed to scrub[16,204,205] as shown in Fig. 48, where a reduction in the measured PY is observed after intense WL SR exposure equivalent to about one day of LHC run at full operation. Such data have been confirmed by *ad hoc* experiments performed at CERN using EPA (Electron Positron Accumulator in Geneva) as a WL source,[21] and the measured PY reduction is shown in Fig. 49. Note that the PY shown in Fig. 49,[21] is per adsorbed photon, and not per incident one as always assumed in this review, so that the numerical results cannot be easily compared. What is evident though is that the exposure to WL induces PY reduction by surface modification. Correlate SEY to PY reduction and vice versa requires some not trivial

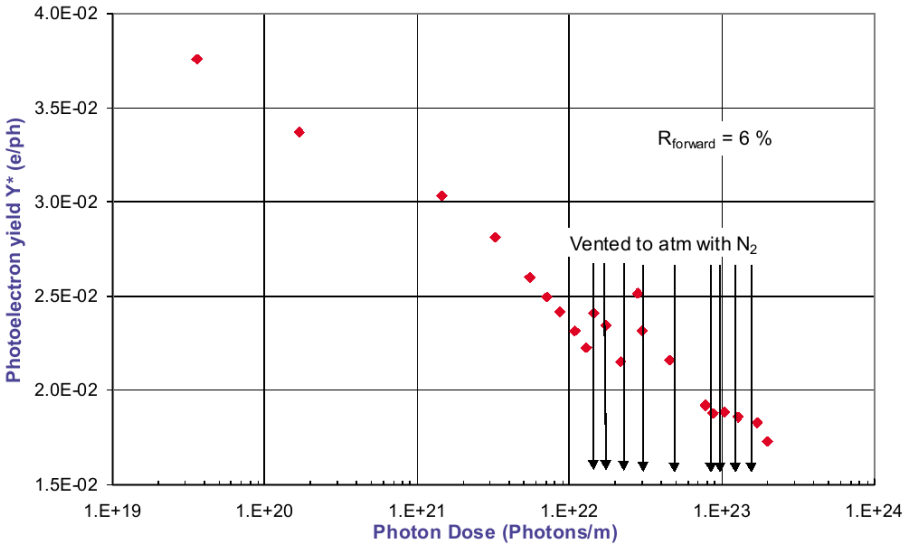

Fig. 49. Photoelectron yield per adsorbed photon (and not per incident photon) of a copper colaminated sleeve with a sawtooth structure of LHC type, during subsequent irradiation with SR white light radiation with a critical energy of 194 eV at 11 mrad incidence. From Ref. 21, thanks to V. Baglin.

experiments, never done so far, on a setup where it is possible to carefully measure SEY and PY on the same surface after e^- and/or photon irradiation. What has been done and allow us to drawn some preliminary conclusions on this matter is a preliminary XPS analysis performed during photon irradiation of an "as received" Cu sample. This experiment suggests that, during photon irradiation, the secondary tail and the oxygen content decrease, but the C1s signal not only does not change much in intensity but does not significantly shift in binding energy, showing that no carbon sp^3–sp^2 conversion is taking place as reported to occur during high energy e^- scrubbing. This can be understood as follows and may clarify the relationship between photon and e^- scrubbing. Let us first assume that photons do not significantly interact with the chemical species of the over-layer coating the surface, due to their ability to penetrate into the solid. This would imply that photons on their own can only marginally promote any chemical modification of the surface. What interacts with the over-layer species are indeed the emitted photoelectrons, whose energy is quite low as previously discussed and evident from Fig. 48. We know from Fig. 47[114] that low energy electrons are not able to induce significant carbon sp^3–sp^2 conversion and the induced modifications of such low energy e^- may only induce a partial reduction in SEY. This simple reasoning supports the notion that photons do scrub but less efficiently than energetic electrons and suggests that their induced surface modifications are overall very similar to those induced by less than 20 eV electrons. Still, the conclusive analysis of the interplay between SEY and

PY modification by photons and or e^- is still missing and would be very useful to understand and predict ECE related behaviors in accelerators or systems where both phenomena can occur.

Scrubbing, then, continues to be an extremely powerful and important e^- cloud mitigation tool but further study is needed to completely understand its final potential and general applicability.

6. Conclusions

Electron cloud in accelerators is still a fast evolving research field not only for its intrinsic value and scientific interest, its ability to merge synergic competences in different research branches but also for the clear and urgent requirement of working solutions to be adopted to improve and consolidate the performances of many accelerators doing top class research all around the world. The enormous burst in the development of differently oriented simulation codes, the still increasing availability of diagnostics and ECE observations on running machines, the number of growing surface laboratories addressing, with increasing precision and details, the subtle surface properties playing a major role in determining ECE, all these issues point towards a continuous improvement of our present understanding to give the required confidence in proposing and running always more demanding accelerators. We feel though, that the "ultimate" solution and complete understanding of all aspects connected to ECE, are still not available, and more work and efforts, are still needed. In this context, we hope that this review, even if not exhaustive and fully comprehensive, will represent an updated snapshot of most of the present understanding and work done so far on the topic. Also, this review has been written to stimulate further work still necessary to fully understand e^- cloud related effects in accelerators and to share some of our specific understanding, within different research areas (like plasma or satellite physics), which may benefit from it to approach some of their specific, still unsolved, challenges.

Acknowledgments

The authors want to thank all the colleagues who contributed to the field and, even if not directly cited in this review, significantly contributed to the enormous advances in the handling, comprehension and prediction capability developed so far in a very lively and communicative community. A special mention goes to our colleague and friend Francesco Ruggiero (1957–2007), who played a major role in bursting much of the scientific activity around this topic, and deeply influenced the authors also on a personal level. The authors are deeply indebted to V. Baglin, R. Larciprete, G. Rumolo, M. Taborelli and F. Zimmermann, for careful reading of the manuscript and significant suggestions and contributions. Roberto Cimino acknowledges the essential support from the NTA-IMCA project funded by INFN, and CERN for hospitality during the final revision of this manuscript.

References

1. G. D. G. Budker and V. Dudnikov (eds.), *Proc. Int. Symp. on Electron and Positron Storage Rings*, Saclay, France, 1966.
2. G. D. G. Budker and V. Dudnikov, *Sov. At. Energy* **22**, 384 (1967).
3. F. Zimmermann, *Phys. Rev. Spec. Top. Accel. Beams* **7**, 124801 (2004).
4. O. Grobner, The dynamic behaviour of pressure bumps in the ISR, Technical Report CERN-ISR-VA-76-25, CERN (1976).
5. J. Poole, *Proc. Chamonix X*, CERN-SL-2000-001 DI (CERN, 2000).
6. J. Poole, *Proc. Chamonix XI*, CERN-SL-2001-003 DI (CERN, 2001).
7. S. Myers, *Int. J. Mod. Phys. A* **28**, 1330035 (2013).
8. O. Grobner, *Vacuum* **60**, 25 (2001).
9. S. Myers, O. Bruning, P. Collier, P. Lebrun, R. Ostojic, J. Poole and P. Proudlock (eds.), LHC Design Report, CERN-2004-003 (CERN, 2004).
10. O. S. Brüning, P. Collier, P. Lebrun, S. Myers, R. Ostojic, J. Poole and P. Proudlock (eds.), LHC Design Report, Technical Report, CERN-2004-003-V-1 (CERN, 2004).
11. G. Arduini, K. Cornelis, G. Hoefle, W. Rumolo and F. Zimmermann, in *Proc. PAC 2001*, CERN-SL-2001-0050 (CERN, 2001).
12. G. Rumolo, in *Proc. ECLOUD'12*, CERN-2013-002 (2013), p. 19.
13. J. D. Jackson, *Classical Electrodynamics* (Wiley Eastern, 1975).
14. E. Koch, *Handbook on Synchrotron Radiation* (North-Holland, 1983).
15. V. Baglin *et al.*, LHC Project Report 188, CERN (1998).
16. R. Cimino, I. R. Collins and V. Baglin, *Phys. Rev. Spec. Top. Accel. Beams* **2**, 063201 (1999).
17. N. Mahne, V. Baglin, I. Collins, A. Giglia, L. Pasquali, M. Pedio, S. Nannarone and R. Cimino, *Appl. Surf. Sci.* **235**, 221 (2004).
18. R. Cimino, *Nucl. Instrum. Methods Phys. Res. A* **561**, 272 (2006).
19. R. Cimino, in *Proc. 31st ICFA Advanced Beam Dynamics Workshop on Electron-Cloud Effects ECLOUD 04* (2004).
20. R. Cimino and I. R. Collins, *Appl. Surf. Sci.* **235**, 231 (2004).
21. V. Baglin, I. R. Collins, O. Gröbner, C. Grünhagel, B. Henrist, N. Hilleret and B. Jenninger, in *Proc. Chamonix XI*, CERN-SL-2001-003 DI (CERN, 2001).
22. Y. Suetsugu, K. Kanazawa, K. Shibata, H. Hisamatsu, K. Oide, F. Takasaki, R. Dostovalov, A. Krasnov, K. Zolotarev, E. Konstantinov, V. Chernov, A. Bondar and A. Shmakov, *Nucl. Instrum. Methods Phys. Res. A* **554**, 92 (2005).
23. Y. Suetsugu, K. Kanazawa, K. Shibata and H. Hisamatsu, *Nucl. Instrum. Methods Phys. Res. A* **556**, 399 (2006).
24. Y. Suetsugu, K. Kanazawa, K. Shibata and H. Hisamatsu, *Nucl. Instrum. Methods Phys. Res. A* **578**, 470 (2007).
25. V. Baglin, G. Bregliozzi, J. Jimenez and G. Lanza, in *Proc. IPAC-2011* (2011), p. 1563.
26. Y. K. Kim *et al.*, *Electron-Impact Ionization Cross Section for Ionization and Excitation Database*, Version 3.0 (National Institute of Standard and Technology, 2004).
27. P. Thieberger, A. L. Hanson, D. B. Steski, V. Zajic, S. Y. Zhang and H. Ludewig, *Phys. Rev. A* **61**, 042901 (2000).
28. J. S. Berg, LHC Project Note 97, CERN (1997).
29. G. Rumolo and F. Zimmermann, CERN Report No. SL-Note-2002-016, CERN (2002), see also The ECLOUD Program, http://wwwslap.cern.ch/collective/electron-cloud/Programs/Ecloud/ecloud.html.
30. H. Seiler, *J. Appl. Phys.* **54**, R1 (1983).

31. O. Gröbner, Bunch induced multipacting, in *10th Int. Conf. on High Energy Accelerators*, Protvino, 1997.
32. G. Stupakov, LHC Project Report 141, CERN (1997).
33. L. Vos, LHC Project Note 150, CERN (1998).
34. S. Heifets, in *Proc. ECLOUD02*, Geneva, 2002.
35. J. Jimenez, G. Arduini, P. Collier, G. Ferioli, B. Henrist, N. Hilleret, L. Jensen, K. Weiss and F. Zimmermann, Electron cloud with LHC-type beams in the SPS: A review of three years of measurements, in *ECLOUD'02 Proceedings* (2002).
36. L. F. Wang, H. Fukuma, K. Ohmi, S. Kurokawa, K. Oide and F. Zimmermann, Electron cloud effects at KEKB, in *ECLOUD'02 Proceedings* (2002).
37. L. Wang *et al.*, *Phys. Rev. Spec. Top. Accel. Beams* **5**, 124402 (2002).
38. M. Billing *et al.*, arXiv:1309.2625 [physics.acc-ph].
39. R. Cimino, I. R. Collins, M. A. Furman, M. Pivi, F. Ruggiero, G. Rumolo and F. Zimmermann, *Phys. Rev. Lett.* **93**, 014801 (2004).
40. R. W. Hockney and J. W. Eastwood, *Computer Simulation Using Particles* (Taylor & Francis, 1988).
41. G. L. M. Furman, The electron-cloud instability in the arcs of the PEP-II positron ring, in *Proc. MBI97*, Tsukuba, Japan, 1997.
42. M. A. Furman and M. F. Pivi, *Phys. Rev. Spec. Top. Accel. Beams* **5**, 124404 (2002).
43. F. Zimmermann, LHC Project Report 95, CERN (1997).
44. W. Fischer, J. M. Brennan, M. Blaskiewicz and T. Satogata, *Phys. Rev. ST Accel. Beams* **5**, 124401 (2002).
45. L. Wang, User's Guide for CLOUDLAND, KEK Internal Report 2003-2, KEK (2003).
46. G. Iadarola and G. Rumolo, in *Proc. ECLOUD'12*, CERN-2013-002 (2013), p. 189.
47. W. Bruns, D. Schulte and F. Zimmermann, in *Proc. EPAC 06* (2006), p. 2223.
48. K. Ohmi, *Phys. Rev. Lett.* **75**, 1526 (1995).
49. Care hhh electron cloud code collection, https://oraweb.cern.ch/pls/hhh/code; website.disp category?catname=Electron%20Cloud.
50. F. Zimmermann, in *Proc. ECLOUD02*, Geneva, 2002.
51. T. Demma, in *Proc. ECLOUD'12*, CERN-2013-002 (2013), p. 43.
52. D. Schulte *et al.*, in *Proc. PAC'05* (2005), p. 1371.
53. A. Pertica and S. J. Payne, in *Proc. ECLOUD'12*, CERN-2013-002 (2013), p. 237.
54. J. A. Crittenden and J. P. Sikora, in *Proc. ECLOUD'12*, CERN-2013-002 (2013), p. 241.
55. O. Dominguez and F. Zimmermann, in *Proc. ECLOUD'12*, CERN-2013-002 (2013), p. 79.
56. V. Baglin, I. Collins, C. Grunhagel, O. Grobner and B. Jenninger, Technical Report, CERN (2000).
57. S. De Santis, J. M. Byrd, F. Caspers, A. Krasnykh, T. Kroyer, M. T. F. Pivi and K. G. Sonnad, *Phys. Rev. Lett.* **100**, 094801 (2008).
58. U. Iriso and S. G. Peggs, *Phys. Rev. Spec. Top. Accel. Beams* **8**, 024403 (2005).
59. T. Demma, S. Petracca, F. Ruggiero, G. Rumolo and F. Zimmermann, *Phys. Rev. Spec. Top. Accel. Beams* **10**, 114401 (2007).
60. T. Demma, S. Petracca and R. Cimino, in *Proc. PAC'09* (2009), p. 4698.
61. C. Domínguez and F. Zimmermann, in *Proc. IPAC'13* (2013), p. 1451.
62. U. Iriso and S. Peggs, *Phys. Rev. ST Accel. Beams* **9**, 071002 (2006).
63. U. Iriso and S. G. Peggs, in *Proc. EPAC'06* (2006), pp. 357–359.
64. T. Demma and S. Petracca, in *Proc. EPAC'08* (2008), pp. 1601–1603.

65. S. Petracca, A. Stabile and T. Demma, in *Proc. ECLOUD'12*, CERN-2013-002 (2013), pp. 231–236.
66. K. Ohmi, S. Heifets and F. Zimmermann, in *Proc. APAC 2001.*
67. G. Dugan *et al.*, in *Proc. ECLOUD'12*, CERN-2013-002 (2013), p. 31.
68. G. Dugan and D. Sagan, in *Proc. ECLOUD'12*, CERN-2013-002 (2013), p. 117.
69. M. Izawa, Y. Sato and T. Toyomasu, *Phys. Rev. Lett.* **74**, 5044 (1995).
70. Z. Y. Gou *et al.*, in *Proc. PAC99* (1999).
71. S. S. Win, K. Ohmi, H. Fukuma, M. Tobiyama, J. Flanagan and S. Kurokawa, *Phys. Rev. Spec. Top. Accel. Beams* **8**, 094401 (2005).
72. T. Demma, *ICFA Beam Dyn. Newslett.* **48**, 64 (2009).
73. G. Arduini, in *Proc. Chamonix XI*, SL-2001-003 DI (CERN, 2001).
74. M. Bassetti and G. Erskine, Technical Report, CERN-ISR-TH/80-06, CERN (1980).
75. A. Chao, *Physics of Collective Beam Instabilities in High Energy Accelerators* (Wiley, 1993).
76. K. Ohmi, in *Proc. ECLOUD'12*, CERN-2013-002 (2013), p. 219.
77. K. Ohmi, in *Proc. ICAP2012* (2012), p. 28.
78. E. Benedetto, G. Franchetti and F. Zimmermann, *Phys. Rev. Lett.* **97**, 034801 (2006).
79. G. Franchetti, I. Hofmann, W. Fischer and F. Zimmermann, *Phys. Rev. Spec. Top. Accel. Beams* **12**, 124401 (2009).
80. G. Franchetti and F. Zimmermann, *Phys. Rev. Lett.* **109**, 23412 (2012).
81. K. Ohmi and F. Zimmermann, *Phys. Rev. Lett.* **85**, 3821 (2000).
82. K. Ohmi, F. Zimmermann and E. Perevedentsev, *Phys. Rev. E* **65**, 016502 (2001).
83. K. Ohmi, in *Proc. 31st ICFA Advanced Beam Dynamics Workshop*: *Electron-Cloud Effects* (*ECLOUD 04*), USA, 2004.
84. K. Ohmi, in *Proc. PAC01* (2001), p. TPPH096.
85. G. Rumolo and F. Zimmermann, *Phys. Rev. Spec. Top. Accel. Beams* **5**, 121002 (2002).
86. Code Web Repository, http://www-linux.gsi.de/?giuliano/micromap/manmimac_tmp.html.
87. M. T. F. Pivi, in *Proc. PAC07* (2007), p. THPAS066.
88. J.-L. Vay *et al.*, in *Proc. PAC09* (2009), p. FR5RFP078.
89. C. Nieter and J. R. Cary, *J. Comput. Phys.* **196**, 448 (2004).
90. K. Sonnad *et al.*, in *Proc. ECLOUD'10* (2010), p. 100.
91. P. C. Marin, Designing accelerator vacuum systems, CAS-CERN Accelerator School: Vacuum technology CERN-99-05 (1999).
92. D. Garton, Vacuum technology and vacuum design handbook for accelerator technicians, No. ANSTO-E-775 (Australian Nuclear Science and Technology Organization, 2011).
93. A. Chao, K. H. Mess, M. Tigner and F. Zimmermann, *Handbook of Accelerator Physics and Engineering* (World Scientific, 2013).
94. G. Fubiani, H. P. L. de Esch, A. Simonin and R. S. Hemsworth, *Phys. Rev. Spec. Top. Accel. Beams* **11**, 014202 (2008).
95. C. Chang, H. Shao, C. H. Chen, C. X. Tang and W. H. Huang, *Phys. Plasmas* **17**, 053301 (2010).
96. V. E. Semenov, N. A. Zharova, D. Anderson, M. Lisak and J. Puech, *Phys. Plasmas* **17**, 123503 (2010).
97. S. T. Lai, *Fundamentals of Spacecraft Charging*: *Spacecraft Interactions with Space Plasmas* (Princeton University Press, 2011).
98. D. Raboso, *Proc. MULCOPIM'08 Conference*, 2008.
99. R. Seviour, *IEEE Trans. Electron Devices* **52**, 1927 (2005).

100. R. Seviour, *J. Spacecr. Rockets* **47**, 634 (2010).
101. B. Feuerbacher, B. Fitton and R. Willis, *Photoemission and the Electronic Properties of Surfaces* (Wiley, 1978).
102. G. Panaccione and K. Kobayashi, *Surf. Sci.* **606**, 125 (2012).
103. M. P. Seah and W. A. Dench, *Surf. Interface Anal.* **1**, 2 (2004).
104. A. Shih, J. Yater, C. Hor and R. Abrams, *Appl. Surf. Sci.* **111**, 251 (1997).
105. N. Bundaleski, B. J. Shaw, A. G. Silva, A. M. C. Moutinho and O. M. Teodoro, *Scanning* **33**, 266 (2011).
106. A. J. Dekker, Secondary electron emission, in *Solid State Physics, Advances in Research and Applications*, eds. F. Seitz and D. Turnbull (Academic Press, New York, 1958), p. 251.
107. Y. Lin and D. C. Joy, *Surf. Interface Anal.* **37**, 895 (2005).
108. S. Clerc, J. Dennison, R. Hoffmann and J. Abbott, *IEEE Trans. Plasma Sci.* **34**, 2219 (2006).
109. J. Roupie, O. Jbara, T. Tondu, M. Belhaj and J. Puech, *J. Phys. D*: *Appl. Phys.* **46**, 125306 (2013).
110. K. Besocke, B. Krahl-Urban and H. Wagner, *Surf. Sci.* **68**, 39 (1977).
111. J. Demuth and T. Rhodin, *Surf. Sci.* **45**, 249 (1974).
112. Y. Wan, Y. Li, Q. Wang, K. Zhang and Y. Wu, *Int. J. Electrochem. Sci.* **7**, 5204 (2012).
113. J. Cazaux, *J. Appl. Phys.* **110**, 024906 (2011).
114. R. Cimino, M. Commisso, D. Grosso, T. Demma, V. Baglin, R. Flammini and R. Larciprete, *Phys. Rev. Lett.* **109**, 064801 (2012).
115. R. Larciprete, D. R. Grosso, M. Commisso, R. Flammini and R. Cimino, *Phys. Rev. Spec. Top. Accel. Beams* **109**, 064801 (2012).
116. D. R. Grosso, M. Commisso, R. Cimino, R. Flammini, R. Larciprete and R. Wanzenberg, in *Proc. IPAC2011* (2011), p. 1533.
117. D. R. Grosso, M. Commisso, R. Cimino, R. Larciprete, R. Flammini and R. Wanzenberg, *Phys. Rev. Spec. Top. Accel. Beams* **16**, 051003 (2013).
118. V. Baglin, J. Bojko, O. Gröbner, B. Henrist, N. Hilleret, C. Scheuerlein and M. Taborelli, Technical Report LHC-Project-Report-433, CERN (2000).
119. C. Scheuerlein, B. Henrist, N. Hilleret and M. Taborelli, *Appl. Surf. Sci.* **172**, 95 (2000).
120. V. Baglin, I. Collins, B. Henrist, N. Hilleret and G. Vorlaufer, LHC Project Report 472, CERN (2001).
121. J.-M. Jimenez, G. Arduini, V. Baglin, P. Collier, G. Ferioli, B. Henrist, N. Hilleret, L. Jensen, B. Jenninger, J. M. Laurent, A. Rossi, K. Weiss and F. Zimmermann, in *Particle Accelerator Conference, 2003, PAC 2003* (2003), p. 307.
122. N. Hilleret, C. Scheuerlein and M. Taborelli, *Appl. Phys. A* **76**, 1085 (2003).
123. P. Chiggiato and P. Costa Pinto, *Thin Solid Films* **515**, 382 (2006).
124. C. Yin Vallgren *et al.*, *Phys. Rev. Spec. Top. Accel. Beams* **14**, 071001 (2011).
125. G. A. Haas, *J. Vac. Sci. Technol.* **13**, 479 (1976).
126. M. Belhaj, T. Tondu and V. Inguimbert, *J. Phys. D*: *Appl. Phys.* **42**, 145306 (2009).
127. T. Tondu, M. Belhaj and V. Inguimbert, *J. Vac. Sci. Technol. A*: *Vacuum, Surfaces, and Films* **28**, 1122 (2010).
128. J. Cazaux, *J. Appl. Phys.* **111**, 064903 (2012).
129. J. Wang, P. Wang, M. Belhaj and J.-C. M. Velez, *IEEE Trans. Plasma Sci.* **40**, 2773 (2012).
130. M. Belhaj, J. Roupie, O. Jbara, J. Puech, N. Balcon and D. Payan, in *Proc. ECLOUD'12*, CERN-2013-002 (2013), p. 137.

131. P. G. Park, V. Shifrin, Y. G. Kirn, M.-S. Kim and K.-T. Kim, in *Magnetics Conference, INTERMAG Asia 2005. Digests of the IEEE International*.
132. R. E. Kirby and F. K. King, *Nucl. Instrum. Methods Phys. Res. A* **469**, 1 (2001).
133. I. I. Montero, M. L. Aguilera, D. V. Nistor, L. Galan, L. Gonzalez, D. Raboso, P. Costa Pinto, M. Taborelli, F. Caspers, U. Ulrich and D. Wolk, in *Proc. ECLOUD'12*, CERN-2013-002 (2013), p. 153.
134. G. Rumolo and F. Zimmermann (eds.), *Proc. Int. Workshop on Electron-Cloud Effects* (*ECLOUD'02*), CERN-2002-001 (CERN, Geneva, 2002).
135. M. Furman (ed.), *Proc. 31st ICFA Advanced Beam Dynamics Workshop*: *Electron-Cloud Effects* (*ECLOUD'04*), LBNL, USA, 2004, http://icfa-ecloud04.web.cern.ch/icfa-ecloud04/.
136. H. Fukuma, K. Ohmi and E.-S. Kim, *Proc. Int. Workshop on Electron-Cloud Effects* (*ECLOUD'07*), KEK-Proceedings-2007-012 (KEK, Tsukuba, Japan, 2007), http://airex.tksc.jaxa.jp/pl/dr/AA0063628000/en.
137. R. Cimino, G. Rumolo and F. Zimmermann (eds.), *Proc. Int. Workshop on Electron-Cloud Effects* (*ECLOUD'12*), CERN-2-13-002 (CERN, Geneva, 2012), http://ecloud12.web.cern.ch/ecloud12/.
138. Y. H. Chin (ed.), *Proc. Int. Workshop on Multibunch Instabilities in Future Electron and Positron Accelerators* (*MBI'97*), KEK-Proceedings-1997-17 (KEK, Tsukuba, 1997).
139. *Proc. Int. Workshop on Two-Stream Instabilities in Particle Accelerators and Storage Rings* (KEK, Tsukuba, 2001), http://conference.kek.jp/two-stream/.
140. A. Kuzucan, H. Neupert, M. Taborelli and H. Störi, *J. Vac. Sci. Technol. A* **30**, 051401 (2012).
141. C. Yin Vallgren, Low secondary electron yield carbon coatings for electron cloud mitigation in modern particle accelerators, Ph.D. thesis, Chalmers University, Göteborg, Sweden (2011).
142. C. Benvenuti, J. Cazeneuve, P. Chiggiato, F. Cicoira, A. Escudeiro Santana, V. Johanek, V. Ruzinov and J. Fraxedas, *Vacuum* **53**, 219 (1999).
143. N. Bundaleski, S. Candeias, A. Santos, O. Teodoro and A. Silva, in *Proc. ECLOUD'12*, CERN-2013-002 (2013), p. 149.
144. A. N. Andronov, A. S. Smirnov, I. D. Kaganovich, E. A. Startsev, Y. Raitses and V. I. Demidov, in *Proc. ECLOUD'12*, CERN-2013-002 (2013), p. 161.
145. I. M. Bronshtein and B. S. Fraiman, *Secondary Electron Emission* (Atomizdat, Moscow, Russia, 1969).
146. I. M. Bronshtein and V. Roshchin, *Sov. J. Tech. – Phys.* **3**, 2271 (1958).
147. I. H. Khan, J. P. Hobson and R. Armstrong, *Phys. Rev.* **129**, 1513 (1963).
148. H. Heil and J. V. Hollweg, *Phys. Rev.* **164**, 881 (1961).
149. Z. Yakubova and N. A. Gorbatyi, *Russ. Phys. J.* **13**, 1477 (1970).
150. J. Cazaux, *J. Appl. Phys.* **111**, 064903 (2012).
151. H. Hertz, *Ann. Phys.* **267**, 983 (1887).
152. A. Einstein, *Ann. Phys.* **322**, 132 (1905).
153. S. Hüfner, *Photoelectron Spectroscopy*: *Principles and Applications* (Springer-Verlag, 2003).
154. M. Cardona and L. Ley, *Photoemission in Solids I*: *General Principles* (Springer, 1978).
155. V. Baglin, I. R. Collins and O. Grobner, LHC-Project-Report 206, CERN (1998).
156. V. V. Anashin, I. R. Collins, R. V. Dostovalov, N. V. Fedorov, O. Grobner, A. A. Krasnov, O. B. Malyshev and E. E. Pyata, Magnetic and electric field effects on the

photoelectron emission from prototype LHC beam screen material, LHC-Project-Report 373, CERN (2000).
157. F. Schäfers and R. Cimino, in *Proc. ECLOUD'12*, CERN-2013-002 (2013), p. 105.
158. L. Boon and K. Harkay, in *Proc. ECLOUD'12*, CERN-2013-002 (2013), p. 95.
159. Particle Data Group (J. Beringer *et al.*), *Phys. Rev. D* **86**, 010001 (2012).
160. B. Henke, Low-energy X-ray interaction coefficients: Photoabsorption, scattering and reflection: E 100–2000 Ev z 1–94, in *Atomic Data and Nuclear Data Tables* (Academic Press, 1982).
161. J. H. Hubbell, H. A. Gimm and I. Øverbø, *J. Phys. Chem. Ref. Data* **9**, 1023 (1980).
162. Lbl X-ray Database, http://henke.lbl.gov/optical_constants/.
163. G. Dugan and D. Sagan, in *Proc. ECLOUD'10* (2010).
164. M. A. Palmer *et al.*, in *Proc. 2009 Particle Accelerator Conference*, Vancouver, BC, 2009, p. 4200.
165. P. Beckmann and A. Spizzichino, *The Scattering of Electromagnetic Waves from Rough Surfaces* (Artech House, 1987).
166. J. Ogilvy, *Theory of Wave Scattering from Random Rough Surfaces* (A. Hilger, 1991).
167. C. Scheuerlein, M. Taborelli, N. Hilleret, A. Brown and M. Baker, *Appl. Surf. Sci.* **202**, 57 (2002).
168. R. Kersevan, in *Proc. EPAC'02* (2002), p. 2565.
169. P. Costa Pinto, S. Calatroni, P. Chiggiato, P. Edwards, M. Mensi, H. Neupert, M. Taborelli and C. Yin Vallgren, in *Proc. ECLOUD'12*, CERN-2013-002 (2013), p. 141.
170. KEK B-Factory Design Report, KEK Report No. 95-7, KEK (1995), Sec. 5.5.2.
171. F. Zimmerman, CERN Report No. SL-Note-2000-004, CERN (2000).
172. G. Bregliozzi, V. Baglin, P. Chiggiato, P. Cruikshank, J. Jimenez and G. Lanza, in *Proc. IPAC-2011* (2011), p. 1560.
173. Y. Cai, M. Pivi and M. Furman, *Phys. Rev. Spec. Top. Accel. Beams* **7**, 024402 (2004).
174. L. F. Wang, D. Raparia, J. Wei and S. Y. Zhang, *Phys. Rev. Spec. Top. Accel. Beams* **7**, 034401 (2004).
175. F. Caspers *et al.*, in *Proc. PAC09* (2009), p. 445.
176. J. Conway *et al.*, in *Proc. PAC11* (2011), p. 1250.
177. Y. Suetsugu, H. Fukuma, L. Wang, M. Pivi, A. Morishige, Y. Suzuki, M. Tsukamoto and M. Tsuchiya, *Nucl. Instrum. Methods Phys. Res. A* **598**, 372 (2009).
178. Y. Suetsugu, H. Fukuma, M. Pivi and L. Wang, *Nucl. Instrum. Methods Phys. Res. A* **604**, 449 (2009).
179. D. Alesini, A. Drago, A. Gallo, S. Guiducci, C. Milardi, A. Stella, M. Zobov, S. De Santis, T. Demma and P. Raimondi, *Phys. Rev. Lett.* **110**, 124801 (2013).
180. A. A. Krasnov, *Vacuum* **73**, 195 (2004).
181. G. Stupakov and M. Pivi, SLAC Report No. SLAC-TN-2004-045, SLAC (2004).
182. L. Wang, T. Raubenheimer and G. Stupakov, *Nucl. Instrum. Methods A* **571**, 588 (2007).
183. M. T. F. Pivi, F. K. King, R. E. Kirby, T. Markiewicz, T. O. Raubenheimer, J. Seeman and L. Wang, SLAC Report No. SLAC-PUB-13284, SLAC (2008).
184. M. T. F. Pivi *et al.*, *J. Appl. Phys.* **104**, 104904 (2008).
185. I. Montero *et al.*, in *Proc. ECLOUD'12*, CERN-2013-002 (2013), p. 153.
186. M. Ye, Y. N. He, S. G. Hu, R. Wang, T. C. Hu, J. Yang and W. Z. Cui, *J. Appl. Phys.* **113**, 074904 (2013).
187. B. Henrist, N. Hilleret, C. Scheuerlein, M. Taborelli and G. Vorlaufer, LHC Project Report 583, CERN (2002).

188. V. Baglin, I. Collins, B. Henrist, N. Hilleret and G. Vorlaufer, A summary of main experimental results concerning the secondary electron emission of copper, LHC-Project-Report 472, CERN (2001).
189. A. Cho, *Science* **338**, 1524 (2012).
190. M. Della Negra, P. Jenni and T. S. Virdee, *Science* **338**, 1560 (2012).
191. CMS Collab., *Science* **338**, 1569 (2012).
192. ATLAS Collab., *Science* **338**, 1576 (2012).
193. M. A. Palmer (ed.), *Proc. 49th Advanced Beam Dynamics Workshop on Electron Cloud Physics* (*ECLOUD'10*) (2010).
194. R. Kirby and F. King, SLAC Report No. SLAC-PUB-8212, SLAC (2000).
195. M. Nishiwaki and S. Kato, *Shinku* **48**, 118 (2005).
196. M. Nishiwaki and S. Kato, *J. Vac. Sci. Technol. A* **25**, 675 (2007).
197. M. Nishiwaki and S. Kato, *Vacuum* **84**, 743 (2009).
198. L. Calliari, M. Filippi and N. Laidani, *Surf. Interface Anal.* **36**, 1126 (2004).
199. F. Banhart, *Rep. Prog. Phys.* **62**, 1181 (1999).
200. C. R. Arumainayagam, H.-L. Lee, R. B. Nelson, D. R. Haines and R. P. Gunawardane, *Surf. Sci. Rep.* **65**, 1 (2010).
201. J. Diaz, G. Paolicelli, S. Ferrer and F. Comin, *Phys. Rev. B* **54**, 8064 (1996).
202. A. Nikitin, L. Näslund, Z. Zhang and A. Nilsson, *Surf. Sci.* **602**, 2575 (2008).
203. R. Larciprete, S. Fabris, T. Sun, P. Lacovig, A. Baraldi and S. Lizzit, *J. Am. Chem. Soc.* **133**, 17315 (2011).
204. V. Baglin *et al.*, in *Proc. EPAC'98* (1998), p. 359.
205. Y. Suetsugu, M. Tsuchiya, T. Nishidono, N. Kato, N. Satoh, S. Endo and T. Yokoyama, *J. Vac. Sci. Technol. A* **21**, 186 (2003).